

Black hole jets on the scale of the Cosmic Web

Martijn S.S.L. Oei^{1,2}, Martin J. Hardcastle³, Roland Timmerman^{1,4}, Aivin R.D.J.G.I.B. Gast⁵, Andrea Botteon⁶, Antonio C. Rodriguez², Daniel Stern⁷, Gabriela Calistro Rivera^{8,9}, Reinout J. van Weeren¹, Huub J.A. Röttgering¹, Huib T. Intema¹, Francesco de Gasperin⁶, and S.G. Djorgovski²

¹*Leiden Observatory, Leiden University, Niels Bohrweg 2, Leiden, 2333 CA, Zuid-Holland, the Netherlands*

²*Cabill Center for Astronomy and Astrophysics, California Institute of Technology, 1216 E California Blvd, Pasadena, CA 91125, California, the United States*

³*Centre for Astrophysics Research, University of Hertfordshire, College Lane, Hatfield, AL10 9AB, Hertfordshire, the United Kingdom*

⁴*Centre for Extragalactic Astronomy, Department of Physics, Durham University, Durham, DH1 3LE, the United Kingdom*

⁵*Somerville College, University of Oxford, Woodstock Road, Oxford, OX2 6HD, Oxfordshire, the United Kingdom*

⁶*INAF-IRA, Via P. Gobetti 101, 40129, Bologna, Italy*

⁷*Jet Propulsion Laboratory, California Institute of Technology, 4800 Oak Grove Drive, Mail Stop 264-789, Pasadena, CA 91109, the United States*

⁸*European Southern Observatory, Karl-Schwarzschild-Strasse 2, 85748, Garching bei München, Germany*

⁹*German Aerospace Center (DLR), Institute of Communications and Navigation, Wessling, Germany*

Summary Paragraph

When sustained for megayears [1, 2], high-power jets from supermassive black holes become the Universe’s largest galaxy-made structures [3]. By pumping electrons, atomic nuclei, and magnetic fields into the intergalactic medium, these energetic flows affect the distribution of matter and magnetism in the Cosmic Web [4–6], and could have a sweeping cosmological influence if they reached far at early epochs. For the last fifty years, the known size range of black hole jet pairs terminated at 4.6–5.0 Mpc [7–9], or 20–30% of a cosmic void radius in the Local Universe [10]. An observational lack of longer jets, as well as theoretical results [11], thus suggested a growth limit at ~ 5 Mpc [12]. Here we report observations of a radio structure spanning ~ 7 Mpc, or $\sim 66\%$ of a coeval cosmic void radius, apparently generated by a black hole between $4.4^{+0.2}_{-0.7}$ –6.3 Gyr after the Big Bang. The structure consists of a northern lobe, a northern jet, a core, a southern jet

with an inner hotspot, and a southern outer hotspot with a backflow. This system demonstrates that jets can avoid destruction by magnetohydrodynamical instabilities over cosmological distances, even at epochs when the Universe was $7\text{--}15^{+6}_{-2}$ times denser than it is today. How jets can retain such long-lived coherence is presently unknown.

Keywords: Active galactic nuclei, astrophysical jets, giant radio galaxies, intergalactic medium

To quantify the impact of black hole energy transport on the intergalactic medium (IGM), radio images from the International LOFAR Telescope (ILT) have recently been searched [e.g. 9, 13–15] for Mpc-scale galactic outflows. In particular, our team systematically scanned the ILT’s ongoing northern sky survey at wavelength $\lambda = 2.08$ m both with machine learning and by eye — the latter with significant contributions from citizen scientists [16]. This endeavour has increased the number of known Mpc-scale outflows from a few hundred to over eleven thousand [15]. Our largest find is the outflow shown in Fig. 1 and Extended Data Fig. 1, which we name Porphyrion. The source, of angular length $\phi = 13.4' \pm 0.1'$, appears unusually thin. To investigate from which galaxy along the jet axis the outflow originates, we processed ILT very-long-baseline interferometry (VLBI) data of the central $4' \times 4'$. At a spatial resolution of 3 kpc, the image (Fig. 1’s top panel inset and Extended Data Fig. 2) shows lone, unresolved radio sources in two galaxies, in both cases implying active accretion onto a supermassive black hole (SMBH). Because the detection of jets near either black hole (and along the overarching NNE–SSW axis) would clarify Porphyrion’s origin, we performed deep follow-up observations with the Upgraded Giant Metrewave Radio Telescope (uGMRT) at $\lambda = 0.46$ m. The resulting image and ancillary DESI Legacy Imaging Surveys (Legacy) optical–infrared data (Fig. 1’s bottom panel) reveal that the outflow protrudes from a massive ($M_{\star} = 6.7^{+1.4}_{-1.4} \cdot 10^{11} M_{\odot}$) galaxy. This is visually clear in Fig. 2, which is processed to highlight the radio morphologies of the two central galaxies. Of these, the southernmost galaxy uniquely displays a 5σ extension along Porphyrion’s overarching jet axis. We observed this galaxy with the Low Resolution Imaging Spectrometer (LRIS) on the W. M. Keck Observatory’s Keck I

Telescope, measuring a spectroscopic redshift $z = 0.896 \pm 0.001$ (Fig. 3’s top panel). We witness Porphyryon at $t_{\text{BB}} = 6.3$ Gyr after the Big Bang.

The outflow’s angular length and redshift entail a sky-projected length $l_p = 6.43 \pm 0.05$ Mpc. This makes Porphyryon the projectively longest known structure generated by an astrophysical body. The outflow’s total length exceeds this projected length, but by how much depends on the unknown inclination of the jets with respect to the sky plane. Deprojection formulae [14] predict a total length $l = 6.8^{+1.2}_{-0.3}$ Mpc, with expectation $\mathbb{E}[L \mid L_p = l_p] = 7.28 \pm 0.05$ Mpc (Methods). We thus estimate Porphyryon to be ~ 7 Mpc long in total. Spanning $\sim 66\%$ of the radius of a typical cosmic void at its redshift, the outflow is truly cosmological. Surprisingly, SMBH jets can remain collimated over several megaparsecs, despite the growth of (magneto)hydrodynamical (MHD) instabilities — chiefly Kelvin–Helmholtz instabilities — predicted theoretically and seen in simulations of shorter jets [e.g. 11]. Similarly, prolonged entrainment of mass from the IGM, even at $z \gtrsim 1$, does not necessarily destabilise jets. No MHD simulations of Mpc-scale jets yet exist: the spatio-temporal grids required imply a numerical cost $\sim 10^2$ times higher than that of state-of-the-art runs. Outflows like Porphyryon thus offer a window into a jet physics regime that, at present, cannot be explored numerically.

Active galactic nuclei (AGN) with accretion disks extending to the innermost stable circular orbits of their SMBHs efficiently convert the gravitational potential energy of infalling matter into radiation, and are thus called radiatively efficient (RE); all others are called radiatively inefficient (RI) [17, 18]. In RE AGN, the luminous accretion disk photo-ionises a circumnuclear region emitting narrow, and often forbidden, spectral lines. The Keck-observed prominence of forbidden ultraviolet–optical lines from oxygen and neon (chiefly that of the [O III] λ_{5007} line, which is 10.3 ± 0.2 times brighter than the $H\beta$ line) therefore reveals the presence of an RE AGN [19]. Bayesian inference of the galaxy’s spectral energy distribution (SED; Methods and Fig. 3’s bottom panel) independently suggests the presence of a luminous SMBH accretion disk with an obscuring torus: our model requires these structures to explain the observed infrared (WISE) and near-ultraviolet (Legacy) flux levels, which exceed those possible with cold dust and stars alone.

By contrast, all previous record-length outflows, such as 3C 236 ($l_p = 4.6$ Mpc; [7]), J1420–0545 ($l_p = 4.9$ Mpc; [8]), and Alcyoneus ($l_p = 5.0$ Mpc; [9]), are fuelled by RI AGN in recent history ($t_{\text{BB}} = 10.2\text{--}12.4$ Gyr). Whereas RI AGN occur primarily in evolved, ‘red and dead’ ellipticals [17], RE AGN feature vigorous gas inflows and are thus generally found in star-forming galaxies. Indeed, in the first billions of years of cosmic time, RE AGN dominated the radio-luminous AGN population [20]. The potential of Mpc-scale outflows to spread cosmic rays, heat, heavy atoms, and magnetic fields through the IGM is particularly high if large specimina could emerge from the type of AGN abundant at early epochs, when the Universe was smaller. The discovery of a 7 Mpc-long, RE AGN-fuelled outflow before cosmic half-time therefore highlights the hitherto understudied cosmological transport capabilities of Mpc-scale outflows.

In the Local Universe, $\sim 30\%$ of all luminous Mpc-scale outflows reside in galaxy clusters, $\sim 60\%$ in galaxy groups, and the remaining $\sim 10\%$ in more dilute parts of filaments, in sheets, or in voids [21]. The Legacy DR10 (shown in Fig. 1’s bottom panel inset) suggests that Porphyrion does not originate from a galaxy cluster: the closest known cluster [22] lies at a comoving distance of 30^{+12}_{-17} Mpc, or 31^{+14}_{-16} cluster radii (Methods). The nearest *Planck* Sunyaev–Zel’dovich detection [23] is $\sim 2^\circ$ away. Concordantly, studies have found that jet-fuelling RE AGN avoid rich environments [24, 25]. In a sphere with a comoving radius of 10 Mpc centred around Porphyrion’s host, we counted 35 ± 6 other Legacy-detected galaxies. By also performing galactic neighbour counts for a control sample of galaxies at comparable redshifts, and by assuming that galactic neighbour counts increase with circumgalactic Cosmic Web density, we estimated Porphyrion’s circumgalactic Cosmic Web density percentile to be $42^{+26}_{-23}\%$ (Methods). This suggests that Porphyrion does not originate from a void. The straightness of the outflow implies a low peculiar speed ($v_p \lesssim 10^2$ km s $^{-1}$), consistent with the host being at the bottom of a local gravitational potential well. The evidence implies that Porphyrion originates from a Cosmic Web filament, and from a galaxy group in particular. Vast voids, which make up the bulk ($\sim 80\%$) of the Universe’s volume [26], surround such structures in most directions. Jets as long as Porphyrion’s thus encounter void-like densities and temperatures with considerable probability. Indeed, the collimated

nature of the jets favours scenarios in which they descend into voids, as jets gain resilience against Kelvin–Helmholtz instabilities when the ambient density declines [e.g. [11](#)]. Dynamical modelling suggests a two-sided jet power $Q = 1.3 \pm 0.1 \cdot 10^{39}$ W and an age $T = 1.9_{-0.2}^{+0.7}$ Gyr (Fig. [4](#); Methods). The outflow’s average expansion speed $v = 0.012 c$, comparable to Alcyoneus’ [\[9\]](#). In voids and the warm–hot IGM, the speed of sound $c_s \sim 10^0\text{--}10^1$ km s $^{-1}$: the jets grow hypersonically at Mach numbers $\mathcal{M} \sim 10^2\text{--}10^3$ and drive strong shocks into voids. Porphyrior’s jets have carried an energy $E = QT = 8_{-1}^{+2} \cdot 10^{55}$ J into the IGM — an amount comparable to the energy released during galaxy cluster mergers [e.g. [27](#)]. This suggests that the outflow is among the most energetic post–Big Bang events to have occurred in its Cosmic Web region. Even though the SMBH might have gained a significant fraction of its mass while powering the jets ($\Delta M_\bullet > 2 \frac{E}{c^2} = 9_{-1}^{+2} \cdot 10^8 M_\odot$), it appears to have maintained a constant spin axis throughout gigayears of activity. Shocks running perpendicular to the jets dissipate enough heat into the filament to increase its temperature by $\Delta T \sim 10^7$ K and its radius by $\Delta r \sim 1$ Mpc (Methods). Outflows like Porphyrior thus locally alter the Cosmic Web’s shape.

Figure [4](#) illustrates that the radio luminosities of Mpc-long outflows with constant jet power initially decrease before stabilising to a jet power–dependent level. Active outflows not only lengthen, but also grow volumetrically [\[15\]](#); consequently, the mean radio luminosity per unit of lobal volume drops over time. In turn, lobal radio surface brightnesses decrease [\[21\]](#), impeding outflow detection [\[14, 15\]](#). As Fig. [1](#) evinces, Porphyrior borders on the noise of leading current-day telescopes; thus, outflows further progressed on the same evolutionary track hitherto evade detection. Similar outflows are likewise undetectable at lower jet powers and at higher redshifts, where increased inverse Compton scattering with the CMB diverts electron energy away from synchrotron radiation — causing lower radio luminosities at fixed jet powers [\[28\]](#). Problematically, cosmological surface brightness dimming further reduces radio surface brightnesses by a factor of $(1 + z)^{3-\alpha}$, where α is the radio spectral index. Statistical modelling [\[14, 15\]](#) indeed suggests that the detectable population is just the tip of the iceberg: owing to their apparent faintness, most Mpc-scale outflows are still concealed by noise. These arguments, and the fact that our search covered only $\sim 15\%$ of the

sky, imply the existence of a hidden population of outflows with sizes comparable to, and possibly larger than, Porphyrior's.

Porphyrior indicates that RE AGN may be at least as effective at generating Mpc-scale outflows as RI AGN are in the Local Universe. If the comoving number density of actively powered Mpc-scale outflows has remained roughly constant over time at $\sim 10^1 (100 \text{ Mpc})^{-3}$ [14, 15], and a comoving volume of $(100 \text{ Mpc})^3$ contains $\sim 10^2$ filaments, then there would exist $\sim 10^{-1}$ actively powered Mpc-scale outflows in every filament at every instant. As their jets endure for $\sim 10^{-2} - 10^0$ Gyr [1, 3, 9], $\sim 10^1$ Mpc-scale outflows may have been generated in every filament throughout cosmic history. If jet powers $Q \sim 10^{38} \text{ W}$ are typical [1, 9, 28], Mpc-scale outflows induce significant heating ($\Delta T \sim 10^6 \text{ K}$) and expansion ($\Delta r \sim 10^{-1} \text{ Mpc}$) of cosmic filaments (Methods), which comprise the Universe's primary baryon reservoir. Whereas AGN feedback has been known to maintain the thermodynamic state in the $\sim 1 \text{ Mpc}^3$ -scale volumes of galaxy clusters, Porphyrior's discovery highlights the importance of black hole energy transport in the Cosmic Web at large.

References

1. Hardcastle, M. J. *et al.* Radio-loud AGN in the first LoTSS data release. The lifetimes and environmental impact of jet-driven sources. *Astron. Astrophys.* **622**, A12 (2019).
2. Perucho, M., Martí, J.-M. & Quilis, V. Long-term FR II jet evolution: clues from three-dimensional simulations. *Mon. Not. R. Astron. Soc.* **482**, 3718–3735 (2019).
3. Dabhade, P., Saikia, D. J. & Mahato, M. Decoding the giant extragalactic radio sources. *Journal of Astrophysics and Astronomy* **44**, 13 (2023).
4. Ayromlou, M., Nelson, D. & Pillepich, A. Feedback reshapes the baryon distribution within haloes, in halo outskirts, and beyond: the closure radius from dwarfs to massive clusters. *Mon. Not. R. Astron. Soc.* **524**, 5391–5410 (2023).
5. Beck, A. M., Hanasz, M., Lesch, H., Remus, R. .- & Staszczyn, F. A. On the magnetic fields in voids. *Mon. Not. R. Astron. Soc.* **429**, L60–L64 (2013).

6. Vazza, F. *et al.* Simulations of extragalactic magnetic fields and of their observables. *Classical and Quantum Gravity* **34**, 234001 (2017).
7. Willis, A. G., Strom, R. G. & Wilson, A. S. 3C236, DA240; the largest radio sources known. *Nature* **250**, 625–630 (1974).
8. Machalski, J., Koziel-Wierzbowska, D., Jamrozy, M. & Saikia, D. J. J1420-0545: The Radio Galaxy Larger than 3C 236. *Astrophys. J.* **679**, 149–155 (2008).
9. Oei, M. S. S. L. *et al.* The discovery of a radio galaxy of at least 5 Mpc. *Astron. Astrophys.* **660**, A2 (2022).
10. Correa, C. M. *et al.* Redshift-space effects in voids and their impact on cosmological tests. Part I: the void size function. *Mon. Not. R. Astron. Soc.* **500**, 911–925 (2021).
11. Perucho, M. Dissipative Processes and Their Role in the Evolution of Radio Galaxies. *Galaxies* **7**, 70 (2019).
12. Andernach, H., Jiménez-Andrade, E. F. & Willis, A. G. Discovery of 178 Giant Radio Galaxies in 1059 deg² of the Rapid ASKAP Continuum Survey at 888 MHz. *Galaxies* **9**, 99 (2021).
13. Dabhade, P. *et al.* Giant radio galaxies in the LOFAR Two-metre Sky Survey. I. Radio and environmental properties. *Astron. Astrophys.* **635**, A5 (2020).
14. Oei, M. S. S. L. *et al.* Measuring the giant radio galaxy length distribution with the LoTSS. *Astron. Astrophys.* **672**, A163 (2023).
15. Mostert, R. I. J. *et al.* Constraining the giant radio galaxy population with machine learning and Bayesian inference. *arXiv e-prints*, arXiv:2405.00232 (2024).
16. Hardcastle, M. J. *et al.* The LOFAR Two-Metre Sky Survey. VI. Optical identifications for the second data release. *Astron. Astrophys.* **678**, A151 (2023).
17. Heckman, T. M. & Best, P. N. The Coevolution of Galaxies and Supermassive Black Holes: Insights from Surveys of the Contemporary Universe. *ARA&A* **52**, 589–660 (2014).
18. Hardcastle, M. Interpreting radiative efficiency in radio-loud AGNs. *Nature Astronomy* **2**, 273–274 (2018).
19. Buttiglione, S. *et al.* An optical spectroscopic survey of the 3CR sample of radio galaxies with $z < 0.3$. II. Spectroscopic classes and accretion modes in radio-loud AGN. *Astron. Astrophys.* **509**, A6 (2010).
20. Williams, W. L. *et al.* LOFAR-Boötes: properties of high- and low-excitation radio galaxies at $0.5 < z < 2.0$. *Mon. Not. R. Astron. Soc.* **475**, 3429–3452 (2018).
21. Oei, M. S. S. L. *et al.* Luminous giants populate the dense Cosmic Web: The radio luminosity-environmental density relation for radio galaxies in action. *arXiv e-prints*, arXiv:2404.17776 (2024).

22. Wen, Z. L. & Han, J. L. A catalog of 1.58 million clusters of galaxies identified from the DESI Legacy Imaging Surveys. *arXiv e-prints*, arXiv:2404.02002 (2024).
23. Planck Collaboration *et al.* Planck 2015 results. XXVII. The second Planck catalogue of Sunyaev-Zeldovich sources. *Astron. Astrophys.* **594**, A27 (2016).
24. Ineson, J. *et al.* Radio-loud Active Galactic Nucleus: Is There a Link between Luminosity and Cluster Environment? *Astrophys. J.* **770**, 136 (2013).
25. Ineson, J. *et al.* The link between accretion mode and environment in radio-loud active galaxies. *Mon. Not. R. Astron. Soc.* **453**, 2682–2706 (2015).
26. Forero-Romero, J. E., Hoffman, Y., Gottlöber, S., Klypin, A. & Yepes, G. A dynamical classification of the cosmic web. *Mon. Not. R. Astron. Soc.* **396**, 1815–1824 (2009).
27. van Weeren, R. J. *et al.* Radio observations of ZwCl 2341.1+0000: a double radio relic cluster. *Astron. Astrophys.* **506**, 1083–1094 (2009).
28. Hardcastle, M. J. A simulation-based analytic model of radio galaxies. *Mon. Not. R. Astron. Soc.* **475**, 2768–2786 (2018).

Figure legends

- 1 **Deep radio images of a 7 Mpc-long, black hole-driven outflow.** These images, (a) and (b), were taken with the ILT and uGMRT at central wavelengths $\lambda = 2.08$ m and $\lambda = 0.46$ m, respectively, and have resolutions of $6.2''$ and $4.3''$. Panel (a)'s inset shows ILT VLBI imagery at $\lambda = 2.08$ m and a resolution of $0.4''$. Panel (b)'s inset shows Legacy DR10 optical-infrared imagery. The larger images cover $15' \times 15'$ of sky, whilst the insets cover $1' \times 1'$. For scale, we show the stellar Milky Way disk (diameter: 50 kpc) and a ten times inflated version. 34

211	2	Radio close-up of Porphyrior's centre. In our imagery, only the southern host	
212		galaxy candidate features an extension along the outflow's overarching jet axis. For	
213		the central $3' \times 3'$ sky area, we show a uGMRT image at $\lambda = 0.46$ m and $3.6''$	
214		resolution. We detect the southern galaxy's radio extension, directed towards the	
215		north-northeast, at 5 s.d. (σ) significance. The contours denote 3σ , 5σ , 10σ , and	
216		100σ	35
217	3	Rest-frame ultraviolet–optical spectroscopy and radio–ultraviolet photom-	
218		etry of the host galaxy. Both demonstrate that Porphyrior arises from an RE	
219		AGN. a) LRIS spectrum exhibiting hydrogen, carbon, oxygen, and neon emis-	
220		sion. The forbidden lines from multiply ionised oxygen and neon (dark red) could	
221		not be generated by even the hottest stars, and instead stem from the narrow-line	
222		region of an RE AGN at a redshift $z = 0.896 \pm 0.001$. b) Bayesian inference	
223		of the galaxy's SED (Methods) favours the presence of an AGN accretion disk	
224		(dark blue) with an obscuring torus (purple), again indicating radiative efficiency.	
225		Residuals are given in multiples of the s.d. (σ).	36
226	4	Measurements overlaid on evolutionary tracks from dynamical modelling.	
227		By superimposing Porphyrior's total length and radio luminosity on these tracks,	
228		we inferred the outflow's two-sided jet power and age. We assumed the host galaxy	
229		to reside in a galaxy group bordering voids, through which the jets eventually	
230		travel. The width and height of Porphyrior's uncertainty ellipse both cover 68%	
231		of probability centred around the median (green dot).	37

Methods

Throughout this work, we assume a flat, inflationary Λ CDM cosmological model with parameters from Planck Collaboration *et al.* [1]: $h = 0.6766$, $\Omega_{\text{BM},0} = 0.0490$, $\Omega_{\text{M},0} = 0.3111$, and $\Omega_{\Lambda,0} = 0.6889$. We define $\Omega_{\text{DM},0} := \Omega_{\text{M},0} - \Omega_{\text{BM},0} = 0.2621$ and $H_0 := h \cdot 100 \text{ km s}^{-1} \text{ Mpc}^{-1}$. Furthermore, we define the spectral index α so that it relates to flux density F_ν at frequency ν as $F_\nu \propto \nu^\alpha$. Under this convention, synchrotron spectral indices are *positive* (i.e. $\alpha = \frac{5}{2}$) for the lowest frequencies and *negative* for higher frequencies. As the restoring PSFs may not be perfectly circular, all reported resolutions are effective resolutions. In other works, Mpc-scale outflows are usually called ‘giant radio galaxies’. (Although Mpc-scale outflows are generated by galaxies, they are not galaxies themselves; therefore, referring to them as a class of ‘galaxies’ could cause confusion. In addition, Mpc-scale outflows may have been primarily studied through radio observations, but their synchrotron losses (like their other radiative losses) appear to have only a minor effect on their evolution [2], suggesting that ‘radio’ should not be used in a name meant to describe these objects intrinsically. Finally, while ‘giant’ appears apt, it is also vague; we thus prefer the more quantitative ‘Mpc-scale’.)

ILT observations and data reduction The International LOFAR Telescope [ILT; 3] is exquisitely sensitive to the metre-wavelength synchrotron radiation generated by electrons and positrons in the first tens to hundreds of megayears after their acceleration to relativistic energies. Consequently, the second data release [DR2; 4] of the LOFAR Two-metre Sky Survey [LoTSS; 5], the ILT’s ongoing northern sky survey in the 120–168 MHz frequency band, has revealed millions of galaxies boasting supermassive black hole (SMBH) jets.

After discovering Porphyrion, the outflow presented in this work, we extracted a total of 16 hours of DDFacet-calibrated visibilities [6] from LoTSS pointings P228+60 and P233+60 (Project ID: LT5-007). (Porphyrion was the son of Ouranos, the Greek primordial sky deity. According to Ps.-Apollodorus, he and Alcyoneus were the greatest of the *Gigantes* (Giants), while Pindar called him the ‘King of the Giants’. He was struck by Zeus’s thunderbolt in the Gigantomachy — the battle between the Giants and the Olympian gods for supremacy over the Cosmos.) Following van Weeren *et al.* [7], we subtracted all sources far away from the target, performed phase shifting and averaging, and self-calibrated the resulting data. This removed residual ionospheric artefacts around ILTJ153004.28+602423.2, the brightest source in the arcminute-scale vicinity of the northern lobe. We

subsequently performed joint deconvolution on the recalibrated target visibilities with WSClean [8] using Briggs weighting -0.5 , yielding the $6.2''$ -resolution image of Fig. 1's top panel. The noise level is $\sigma = 25 \text{ Jy deg}^{-2}$ at its lowest. The outflow appears thin: its width is nowhere more than a few percent of its length. We defined Porphyrior's angular length as the largest possible great-circle distance between a point in the southern hotspot and a point in the northern lobe. The arc connecting these points defines the overarching jet axis, and we measured its position angle to be $27 \pm 1^\circ$.

To investigate the presence of diffuse structure, we applied Gaussian tapering to the weights of the recalibrated target visibilities. The taper's FWHM in the (u, v) -plane was chosen such that the FWHM of the corresponding Gaussian in the sky plane equals $15''$. Again performing deconvolution with WSClean using Briggs weighting -0.5 (albeit in multi-scale mode this time), we obtained the $19.8''$ -resolution image of Extended Data Fig. 1. This image reveals the northern lobe more clearly. The noise level is $\sigma = 4.8 \text{ Jy deg}^{-2}$.

To obtain a high-resolution image of Porphyrior, we reprocessed the P233+60 data, including LOFAR's international stations, from scratch using the LOFAR-VLBI pipeline [9]. This pipeline builds upon the calibration pipeline for the Dutch part of the array to calibrate the international stations. We derived the dispersive phase corrections and gain corrections for the international stations by calibrating against a bright and compact radio source near the target. In this case, we used the aforementioned $\text{ILTJ153004.28+602423.2}$, a known source from the Long-Baseline Calibrator Survey [LBCS; 10, 11]. To reduce interference from unrelated radio sources in Porphyrior's angular vicinity, we phased up LOFAR's core stations to narrow down the field of view and only considered data from long baselines to calculate the calibration solutions. With the calibration solutions applied in the direction of the target, we again performed deconvolution with WSClean (but using Briggs weighting 0) to obtain a $0.4''$ -resolution image, which we show partially in Fig. 1's top panel inset and fully in Extended Data Fig. 2. The noise level is $\sigma = 2.7 \cdot 10^3 \text{ Jy deg}^{-2}$ at its lowest. This image, which covers the central one-third of the total jet system, reveals synchrotron emission at 42σ significance from active galactic nuclei (AGN) in only two galaxies, $19''$ apart. Both lie along the outflow's jet axis nearly halfway between its endpoints. We considered these galaxies, $\text{J152933.03+601552.5}$ and $\text{J152932.16+601534.4}$, to be Porphyrior's host candidates. In contrast to other radio-emitting structures along Porphyrior's axis, such as the southern complex interpreted as an inner hotspot, these candidates have optical counterparts in Legacy Surveys DR10 imagery (see Fig. 1's bottom panel

inset).

uGMRT observations and data reduction On 13 May 2023, we observed the outflow with the Upgraded Giant Metrewave Radio Telescope [uGMRT; 12] in Band 4 (550–750 MHz) for a total of 10 hours. On 23 September 2023, we extended these observations with another 5 hours. These observations are part of GMRT Observing Cycle 44 and have project code 44_101. We requested to record both narrow-band (GSB) and wide-band (GWB) data. Adverse ionospheric conditions during the September run prohibited us from improving upon the images produced with the May run data only. In what follows, we therefore exclusively discuss May run data reduction and results. We performed calibration with Source Peeling and Atmospheric Modeling [SPAM; 13], starting out with the GSB data. After direction-dependent calibration, we used Python Blob Detection and Source Finder [PyBDSF; 14] to derive a sky model from the final GSB image, which subsequently served to initialise the direction-dependent calibration of the GWB data. As SPAM was designed with narrow-band data in mind, following standard practice, we first split the GWB data along the frequency axis, yielding four subbands of 50 MHz width each. We then calibrated each subband independently. A joint image of four calibrated subbands revealed residual ionospheric artefacts from ILTJ153004.28+602423.2, the same bright source in the vicinity of the northern lobe mentioned earlier. To mitigate these artefacts, we subtracted (on a subband basis) all sources outside of a spherical cap with a $9'$ radius centred around J2000 right ascension $\varphi = 15^{\text{h}}29^{\text{m}}32.0^{\text{s}}$ and declination $\theta = 60^{\circ}15'33.0''$. We then jointly reimaged the four source-subtracted subbands with WSClean, using Briggs weighting 0. This resulted in the $4.3''$ -resolution image of Fig. 1's bottom panel. The noise level is $\sigma = 3 \text{ Jy deg}^{-2}$ at its lowest.

In the Legacy Survey DR10 optical imagery shown in Fig. 1's bottom panel inset, we identified two faint galaxies in the arcsecond-scale vicinity of the southern host galaxy candidate. Of these, the galaxy at $(\varphi, \theta) = (232.37969^{\circ}, 60.26029^{\circ})$ emits low-frequency radio emission at 6σ significance. At the $4.3''$ resolution of our fiducial uGMRT image, this radio emission is only narrowly separable from the host galaxy candidate's, thus interfering with establishing the radio morphology of the candidate. Trading depth for resolution, we reimaged the uGMRT data with WSClean using Briggs weighting -0.5 , yielding a $3.6''$ resolution. Subsequently, to isolate the radio morphology of J152932.16+601534.4, we fit a circular Gaussian fixed at the sky coordinates of its radio-emitting neighbour. Naturally, we set this Gaussian's full width at half maximum to $3.6''$. Upon

312 subtracting the Gaussian, we obtained our final image; Fig. 2 shows its central region, where the noise level is
313 $\sigma = 6 \text{ Jy deg}^{-2}$ at its lowest. Only the southern (and most radio-luminous) host galaxy candidate features
314 an extension along the overarching jet axis seen in Fig. 1. (Radio luminosity L_ν is, at fixed redshift and large-
315 scale halo mass, approximately proportional to jet power Q [2]. Under the Blandford–Znajek mechanism [15],
316 $Q \propto M_\bullet^2$ (at fixed magnetic field strength and spin), where M_\bullet is the SMBH mass. As the generation of Por-
317 phyrion’s jets entails a significant SMBH mass gain $\Delta M_\bullet \sim 10^8\text{--}10^9 M_\odot$, the SMBH must now be massive;
318 hence, a high radio luminosity is expected.) In our data, this extension — indicative of a pair of relativistically
319 beamed jets — occurs at 5σ significance.

320 We estimated the probability to find a spurious (i.e. unrelated) radio-luminous AGN (RLAGN) with jets
321 along Porphyrion’s overarching axis in the region where the host galaxy could plausibly reside. To find the sky
322 density of RLAGN with discernible jet orientations at arcsecond-scale resolutions, metre-scale wavelengths, and
323 10^1 Jy deg^{-2} -scale noise levels, we studied the LoTSS DR1-derived RLAGN sample presented in Hardcastle
324 *et al.* [16]. This sample, consisting of 23,344 RLAGN, contains 6,850 RLAGN with discernible jet orientations.
325 The latter population’s *average* sky density $\bar{n}_s = 4 \cdot 10^{-3} \text{ arcmin}^{-2}$. Approximating the sky density n_s of
326 spurious RLAGN with discernible jet orientations near Porphyrion’s host with \bar{n}_s would be appropriate only
327 if such RLAGN would not cluster in the sky. More optimally, we estimated n_s by first counting, for each such
328 RLAGN (that appears sufficiently far from the edges of the survey footprint), the number of neighbours in
329 disks of radius $1'$. Next, we divided each count by the solid angle of the disks, and finally determined the sample
330 mean: $n_s = 8 \cdot 10^{-3} \text{ arcmin}^{-2}$. (For disks of larger radii, n_s approaches \bar{n}_s .) We estimated the solid angle of the
331 ‘strip’ in which an unrelated source could be mistaken for Porphyrion’s host to be $\Omega_s = 10^0 \times 10^{-1} \text{ arcmin}^2$.
332 (We limited the strip’s angular length by asserting that plausible host candidates lie between Porphyrion’s two
333 detected patches of jet emission.) Defining jets ‘aligned’ with Porphyrion’s when their position angle falls within
334 a range of width 10^1 deg centred around Porphyrion’s position angle, the probability of randomly attaining
335 alignment $p_s = \frac{10^\circ}{180^\circ} = 6 \cdot 10^{-2}$. One thus expects to encounter $\mathbb{E}[N_s] = n_s \cdot \Omega_s \cdot p_s = 4 \cdot 10^{-5}$ unrelated
336 RLAGN with resolved and aligned jets near Porphyrion’s host. Assuming that N_s is Poisson-distributed, one or
337 more such spurious sources appear with a probability $\mathbb{P}(N_s \geq 1) = 1 - e^{-\mathbb{E}[N_s]} \approx \mathbb{E}[N_s]$. (This approximation
338 improves as $\mathbb{E}[N_s]$ decreases.) We thus find $\mathbb{P}(N_s \geq 1) = 4 \cdot 10^{-5}$; the probability to find a spurious *unresolved*

RLAGN in the same region is $4 \cdot 10^1$ times larger. We conclude that J152932.16+601534.4 is Porphyrion’s host galaxy.

Keck I observations and data reduction The literature offers only photometric redshift estimates of the host galaxy. The SDSS DR12 [17] reports $z_p = 0.68 \pm 0.06$, the Legacy Surveys DR9 [18] reports $z_p = 0.93 \pm 0.08$, and Duncan [19] reports $z_p = 0.92 \pm 0.08$. For radio-emitting galaxies like J152932.16+601534.4, we consider the latter estimate to be most reliable.

To establish the redshift of Porphyrion’s host galaxy with certainty, we measured its (rest-frame) ultraviolet–optical spectrum with the Low Resolution Imaging Spectrometer [LRIS; 20–23] on the W. M. Keck Observatory’s Keck I Telescope. Adequate slit placement requires accurate knowledge of the galaxy’s coordinates. From the Legacy Surveys DR10 best-fit model, we found that J152932.16+601534.4’s centre lies at $(\varphi, \theta) = (232.38410^\circ, 60.25960^\circ)$. The galaxy’s half-light radius is 10.1 ± 0.3 kpc. On 23 June 2023, we observed the galaxy for a total of 900 seconds. We used the 600/4000 grism on LRIS’ blue side, with 1×2 binning (spatial and spectral, respectively), and the 400/8500 grating on the red side, again with 1×2 binning. During the observations, the seeing was approximately $0.8''$; as we used a $1.5''$ slit, minimal slit losses occurred. Using a slit position angle of -70° , we could simultaneously obtain a spectrum for J152933.03+601552.5, the quasar-hosting galaxy which we initially considered (and then discarded) as a host candidate. We reduced the data with PyPeIt [24], a Python-based pipeline with features tailored to reducing LRIS long-slit spectroscopy. We flat-fielded and sky-subtracted the data using standard techniques. We used internal arc lamps for wavelength calibration and a standard star for overall flux calibration.

The final LRIS-derived spectra of J152932.16+601534.4 and J152933.03+601552.5 are shown in Fig. 3 and Extended Data Fig. 3, respectively. The corresponding spectroscopic redshifts are $z_s = 0.896 \pm 0.001$ and $z_s = 0.799 \pm 0.001$. The uncertainties reflect LRIS’ limited spectral resolution as well as systematic errors in wavelength calibration. The latter spectroscopic redshift can be compared to the value derived for J152933.03+601552.5 by the SDSS BOSS [25] on 5 July 2013. Visual inspection of the SDSS BOSS spectrum and its best fit indicates a robust spectroscopic redshift $z_s = 0.79836 \pm 5 \cdot 10^{-5}$. The two measurements are in agreement.

Spectral energy distribution

To further assess the accretion mode of Porphyrion’s AGN, and to estimate its host’s stellar mass and possibly star formation rate (SFR), we performed spectral energy distribution (SED) inference. Through VizieR, the Astro Data Lab, and the NASA/IPAC Extragalactic Database, we collected catalogued total (rather than fixed-aperture) flux densities, relative flux densities, magnitudes, Galactic transmission fractions, and total extinctions from rest-frame ultraviolet to radio wavelengths. Extended Data Fig. 4 shows the crossmatching results. It demonstrates that Porphyrion’s host galaxy (as identified in Legacy DR10) is, in view of the astrometric accuracies of the collected catalogue data, the only plausible match. Just $4.3''$ northeast from Porphyrion’s host galaxy lies another source, which could be either a Milky Way star or a galaxy. Mindful of the possibility of spuriously high flux density measurements as a result of target–neighbour blending, we assessed all images underlying the catalogued estimates by eye. The neighbouring source only appears to be a point of attention for flux density measurements at small wavelengths, such as in the Legacy g - and r -band, where it has flux densities $\sim 100\%$ and $\sim 60\%$ those of the target, respectively. At the Legacy z -band’s larger wavelengths, the neighbour’s flux density is small ($\sim 20\%$) relative to the target’s. The error induced by blending, which will add only a fraction of the neighbour’s flux density, should thus be negligible. Accordingly, the Pan-STARRS and WISE measurements at even larger wavelengths are not compromised by this neighbour.

We converted the Legacy relative flux densities to flux densities by multiplying with the reference flux density $F_\nu = 3631$ Jy. We converted the Pan-STARRS AB magnitudes to flux densities using the standard relation (e.g. Eq. 1 of Chambers *et al.* [26]). We converted the WISE relative flux densities to flux densities by multiplying with the reference flux densities of Jarrett *et al.* [27]’s Table 1. Extended Data Table 1 provides all retained flux densities F_ν and the central wavelengths λ they correspond to.

Porphyrion’s host galaxy lies at a Galactic latitude $b = 47.43194^\circ$. Fortunately, at these latitudes, the Galactic transmission is high for all bands included in our SED inference. We tabulate estimated transmitted fractions f_t in Extended Data Table 1. For Pan-STARRS i and y , we calculated f_t from total extinctions $A_\lambda = 0.022$ and $A_\lambda = 0.014$, respectively, via $f_t = 10^{-\frac{2}{5}A_\lambda}$. For Legacy g , where Galactic transmission is lowest, application of the correction factor f_t^{-1} results in a flux density increase of just $\sim 4\%$. For all bands, the correction is smaller than the flux density uncertainty. We conclude that, for our purposes, Galactic extinction can be neglected.

Next, using AGNfitter [28, 29], we determined the SED posterior shown in the bottom panel of Fig. 3. The

posterior indicates the presence of a luminous SMBH accretion disk with an obscuring torus, confirming the radiatively efficient nature of Porphyrior's AGN. The SED posterior further implies that the stellar mass of Porphyrior's host is $M_\star = 6.7 \pm 1.4 \cdot 10^{11} M_\odot$. To gauge the sensitivity of stellar mass estimates for this galaxy to methodological variation, we compare our result to the corresponding stellar mass estimate in the LoTSS DR2 value-added catalogue [30]. This catalogue's authors derive a stellar mass $M_\star = 5.5^{+0.7}_{-0.6} \cdot 10^{11} M_\odot$ from SED fits to Legacy g , r , z and WISE W_1 and W_2 flux densities. (This stellar mass estimate is not based on the spectroscopic redshift we have obtained through LRIS, but utilises a photometry-based redshift posterior with mean and standard deviation $z_p = 0.92 \pm 0.08$ [19].) The two stellar mass measurements are in agreement. Due to the lack of rest-frame far-infrared photometry, the SFR of Porphyrior's host is virtually unconstrained by the SED posterior.

Radio luminosities and spectral indices To determine metre-wavelength radio luminosities and a metre-wavelength spectral index for Porphyrior, we first measured its flux densities in the $6.2''$ ILT and $4.3''$ uGMRT images. We assumed flux scale uncertainties of 10% and 5%, respectively.

Summing over all structural components, the outflow's total flux density at $\lambda = 2.08$ m is $F_\nu = 63 \pm 6$ mJy. Its total radio luminosity at rest-frame wavelength $\lambda_r = 1.10$ m therefore is $L_\nu = 1.4 \pm 0.1 \cdot 10^{26}$ W Hz $^{-1}$; the core radio luminosity, $L_\nu = 5.3 \pm 0.5 \cdot 10^{24}$ W Hz $^{-1}$, comprises $\sim 4\%$ of the total. The outflow's total flux density at $\lambda = 0.46$ m is $F_\nu = 12.0 \pm 0.6$ mJy. Its total radio luminosity at $\lambda_r = 0.24$ m therefore is $L_\nu = 2.7 \pm 0.1 \cdot 10^{25}$ W Hz $^{-1}$; the core radio luminosity, $L_\nu = 4.7 \pm 0.2 \cdot 10^{24}$ W Hz $^{-1}$, comprises $\sim 17\%$ of the total. These data imply a metre-wavelength total spectral index $\alpha = -1.09 \pm 0.08$ and a core spectral index $\alpha = -0.09^{+0.08}_{-0.07}$. Through spectral index-based interpolation, we estimated the total radio luminosity at $\lambda_r = 2$ m to be $L_\nu = 2.8 \pm 0.3 \cdot 10^{26}$ W Hz $^{-1}$. This latter total radio luminosity is an important input for our dynamical modelling.

We calculated directionally resolved metre-wavelength spectral indices by combining the ILT and uGMRT images. Before doing so, we convolved the latter image to the former's resolution. In Extended Data Fig. 5, we show two regions of interest from the resulting spectral index map, which consequently has a resolution of $6.2''$. To highlight the directions in which our spectral index measurements are informative, we blanked all directions in which the thermal noise-induced spectral index uncertainty exceeds 0.3. The top panel of Extended

418 Data Fig. 5 shows that J152932.16+601534.4, Porphyrior's host galaxy, has a significantly higher spectral index
 419 than J152933.03+601552.5, the aforementioned quasar-hosting galaxy. The former spectral index is consistent
 420 with zero, indicating that the onset of synchrotron self-absorption (SSA) in Porphyrior's host galaxy occurs at
 421 metre wavelengths. By contrast, the onset of SSA in the quasar-hosting galaxy must occur at longer wavelengths,
 422 suggesting a lower lepton energy density and weaker magnetic fields in its synchrotron-radiating region. The
 423 bottom panel of Extended Data Fig. 5 shows that Porphyrior's southern tip features much lower spectral indices,
 424 with a gradient along the jet axis. This gradient is consistent with a scenario of a hotspot with backflow in which
 425 spectral ageing occurs. Whereas $\alpha = -1.0 \pm 0.2$ at the hotspot's southwestern side, the radio spectra gradually
 426 steepen to $\alpha = -1.6 \pm 0.2$ at the hotspot's northeastern side. No spectral trend appears present further
 427 downstream.

428 We investigated more thoroughly whether the metre-wavelength spectral index discrepancy between J152932
 429 .16+601534.4 and J152933.03+601552.5 constitutes evidence that the former galaxy is Porphyrior's host. For each
 430 of the $1.1 \cdot 10^4$ Mpc-scale outflows catalogued by Mostert *et al.* [31], we sought to determine LoTSS DR2 and
 431 VLASS core flux densities. LoTSS DR2 core flux densities were available for 1, 238 Mpc-scale outflows, whilst
 432 VLASS core flux densities were available for 6, 882. We found 924 Mpc-scale outflows for which both core flux
 433 densities were available; for these, we computed 144 MHz–3 GHz spectral indices. Extended Data Fig. 6 sum-
 434 marises the results. The sample mean and standard deviation are -0.25 and 0.33 , respectively; the median is
 435 -0.24 , and 68% of all spectral indices lie between -0.58 and 0.09 . It is likely that some VLASS-detected cores
 436 are undetectable in the LoTSS DR2 because of a combination of low VLASS flux densities and flat ($\alpha \simeq 0$)
 437 or 'inverted' ($\alpha > 0$) radio spectra. The consequence is a bias in Extended Data Fig. 6 towards lower spec-
 438 tral indices. By requiring that the LoTSS DR2 core is an isolated source on the sky, the core spectral indices of
 439 Fanaroff–Riley (FR) I outflows have likely been selected out. As Porphyrior is an FR II outflow, deselecting
 440 FR I outflows may have the beneficial effect of making the distribution more representative of the object under
 441 study here. As shown in Extended Data Fig. 6's inset, the spectral indices in this sample do not exhibit a strong
 442 trend with redshift. Consequently, no major distributional changes occurred when we restricted the sample to
 443 the 254 Mpc-scale outflows whose redshifts differ at most $\Delta z = 0.1$ from those of either J152932.16+601534.4
 444 or J152933.03+601552.5 (Extended Data Fig. 6's golden histogram). We conclude that the known core spectral in-

445 dices of Mpc-scale outflows favour J152932.16+601534.4 over J152933.03+601552.5 as Porphyrion’s host, strength-
 446 ening our earlier identification.

447 **Cosmic Web environment** Cosmic Web environment characterisations of luminous ($L_\nu(\nu = 150 \text{ MHz}) \geq$
 448 $10^{24} \text{ W Hz}^{-1}$) Mpc-scale outflows in the Local Universe ($z \lesssim 0.2$) have recently been obtained [32] by locali-
 449 sation in Bayesian large-scale structure reconstructions and by crossmatching with catalogues of galaxy clusters
 450 ($M_{500} \geq 0.6 \cdot 10^{14} M_\odot$) and galaxy groups ($M_{500} < 0.6 \cdot 10^{14} M_\odot$). The resulting probability distribu-
 451 tion over Cosmic Web environments serves as a prior distribution for Porphyrion’s Cosmic Web environment.
 452 In the Local Universe, $\sim 30\%$ of all luminous Mpc-scale outflows reside in clusters, $\sim 60\%$ in groups, and the
 453 remaining $\sim 10\%$ in more dilute parts of filaments, in sheets, or in voids [32]. Thus, if this probability distri-
 454 bution does not evolve with redshift and a cluster environment can be excluded, Porphyrion likely originates
 455 from a filament. To evaluate whether Porphyrion’s host galaxy inhabits a cluster, we extracted right ascensions,
 456 declinations, redshifts, and R_{500} -radii from the cluster catalogue of Wen & Han [33], which is based on Legacy
 457 DR10. Even though these data allow for cluster detections up to $z \sim 1.5$, we did not find a cluster close to
 458 Porphyrion’s host. To reach this conclusion statistically, we first estimated cluster redshift uncertainties using
 459 $\sigma_z(z) = 0.02 \cdot \frac{z}{0.9} \cdot (1 + z)$ for photometric cluster redshifts, as suggested by the bottom-right panel of Fig. 7
 460 of Wen & Han [33], and $\sigma_z = 0.001$ for spectroscopic cluster redshifts. We neglected uncertainties in cluster
 461 right ascensions and declinations. We then Monte Carlo-simulated a redshift for both Porphyrion’s host and
 462 all clusters (assuming Gaussian redshift distributions), converted right ascensions, declinations, and redshifts
 463 into comoving coordinates, and finally identified the cluster nearest to Porphyrion’s host. We recorded the co-
 464 moving distance to this cluster as well as the ratio between the corresponding proper distance and the cluster’s
 465 R_{500} -radius. We repeated this Monte Carlo procedure millions of times, until the probability distributions over
 466 these distance measures converged. The results are shown in Extended Data Fig. 7. Around Porphyrion’s red-
 467 shift, the Wen & Han [33] photometric cluster redshift uncertainties $\sigma_z \approx 0.04$, large enough to force us to
 468 consider several clusters as candidates for being the nearest. Each peak corresponds to the smallest possible dis-
 469 tance to a possibly nearest cluster. The peak location is determined by both the angle between Porphyrion’s
 470 host and the cluster and by Porphyrion’s redshift. In Monte Carlo realisations such that the cluster redshift
 471 matches Porphyrion’s, the distance is minimal. The nearest cluster lies at a comoving distance of $30^{+12}_{-17} \text{ Mpc}$, or

472 31_{-16}^{+14} cluster radii (68% probability intervals); the nearest cluster lies at a comoving distance of 30_{-22}^{+14} Mpc, or
 473 31_{-23}^{+19} cluster radii (95% probability intervals). In just 0.1% of all realisations, Porphyrion’s host is five or fewer
 474 R_{500} -radii away from the nearest cluster.

475 To investigate whether a filament or a void environment is more probable, we performed probabilistic galaxy
 476 counts using the Legacy data underlying the Wen & Han [33] cluster catalogue. We extracted right ascensions,
 477 declinations, redshift posterior means, and redshift posterior standard deviations of all Legacy-detected galaxies
 478 that lie within 1.5° of Porphyrion’s host. In a similar spirit as before, we then Monte Carlo–simulated redshifts
 479 (where, for simplicity, we approximated the galaxies’ redshift posterior distributions with Gaussian distribu-
 480 tions), converted right ascensions, declinations, and redshifts into comoving coordinates, and counted the num-
 481 ber of Legacy-detected galaxies (excluding Porphyrion’s host) within a sphere of given radius centred around
 482 Porphyrion’s host. To properly take into account galactic redshift uncertainties, we repeated this Monte Carlo
 483 procedure 1, 000 times. In a sphere with a comoving radius of 10 Mpc centred around Porphyrion’s host, we
 484 counted 35 ± 6 other Legacy-detected galaxies. We then performed analogous probabilistic galactic neighbour
 485 counts for a control sample of galaxies at comparable redshifts. We selected controls by demanding that their red-
 486 shift means do not deviate more than 0.05 from Porphyrion’s. To ensure that these mean redshifts are reliable,
 487 we further demanded that the redshift standard deviations of controls are less than 0.1. From the available can-
 488 didate controls, we picked 100 controls at random, and performed the counts for them. Porphyrion’s galactic
 489 neighbour count, relative to those of the control sample, occurs at percentile $42_{-23}^{+26}\%$. If we assume that cir-
 490 cumgalactic Cosmic Web density is a monotonic function of the number of galactic neighbours, Porphyrion’s
 491 circumgalactic Cosmic Web density percentile will be $42_{-23}^{+26}\%$, too. This suggests that Porphyrion does not
 492 originate from a void. In line with the expectation for luminous Mpc-scale outflows in the Local Universe, we
 493 conclude that Porphyrion most likely originates from a filament.

494 **Dynamical modelling: jet power and age** We derived Porphyrion’s jet power and age from its length, ra-
 495 dio luminosity, cosmological redshift, and likely environment by fitting evolutionary tracks. We generated these
 496 evolutionary tracks with the simulation-based analytic outflow model of Hardcastle [2]. This model requires as-
 497 sumptions on the large-scale environment in which the dynamics take place. Following the previous section, we
 498 suppose that the host galaxy resides in the centre of a galaxy group of mass $M_{500} = 10^{13} M_\odot$ (which comprises

contributions from both dark and baryonic matter) [32, 34]. We assigned the group a universal pressure profile [UPP; 35] $p_g(r)$, which can be parametrised just by M_{500} . (Sun *et al.* [36] have shown that the UPP applies to galaxy groups, even though the profile has originally been proposed to fit data on galaxy clusters — which have much higher masses: $10^{14} M_\odot < M_{500} < 10^{15} M_\odot$.) To obtain the group’s baryon density profile from its pressure profile, we invoked the ideal gas law: $\rho_g(r) = \frac{p_g(r)\langle m \rangle}{k_B T_g}$, where $\langle m \rangle$ is the average plasma particle mass and T_g the group temperature. We assumed a pure ^1H – ^4He plasma with a ^4He mass fraction $Y = 25\%$ [e.g. 37], so that $\langle m \rangle \approx \frac{4}{8-5Y} m_p = 0.6 m_p$, where m_p is the proton mass. We estimated T_g , which we assumed constant in space and time, using the mass–temperature relation specified by Eq. 9 and Tables 3 and 4 of Lovisari *et al.* [38]:

$$\frac{k_B T_g}{2 \text{ keV}} = 0.77 \cdot \left(\frac{M_{500}}{5 \cdot 10^{13} h_{70}^{-1} M_\odot} \right)^{0.61}. \quad (1)$$

The aforementioned mass implies $T_g = 7 \cdot 10^6$ K. As Mpc-scale outflows reach beyond the edges of groups, it was also necessary to estimate the pressure and baryon density in the AGN’s more distant surroundings. Following the bottom-right panel of Ricciardelli *et al.* [39]’s Fig. 6, we set the baryon overdensity within voids at Porphyrior’s redshift to $\delta = -0.7$. (In doing so, we implicitly assumed that the baryonic matter overdensity field is identical to the total matter overdensity field — which comprises contributions from both dark and baryonic matter — as Ricciardelli *et al.* [39] considers the latter.) We obtained a void baryon density $\rho_v = \rho_{c,0} \Omega_{\text{BM},0} (1+z)^3 (1+\delta) = 9 \cdot 10^{-31} \text{ g cm}^{-3}$, where $\rho_{c,0}$ is today’s critical density. Following Upton Sanderbeck *et al.* [40]’s detailed study of IGM temperatures through cosmic time, which suggests a void temperature $T_v \sim 10^3$ – 10^4 K at Porphyrior’s redshift, we set $T_v = 1 \cdot 10^4$ K. This choice reflects the fact that we are interested in void temperatures near the galaxy group. Again applying the ideal gas law, and taking $\langle m \rangle$ as before, we obtained a void pressure $p_v = 1 \cdot 10^{-19}$ Pa. Finally, we defined the external pressure $p_e(r) = p_g(r) + p_v$, baryon density $\rho_e(r) = \rho_g(r) + \rho_v$, and baryon density–weighted temperature $T_e(r) = \frac{\rho_g(r)T_g + \rho_v T_v}{\rho_e(r)}$. Extended Data Fig. 8 shows these profiles.

We explored whether the addition of a filament component would significantly change Extended Data Fig. 8’s profiles. We assumed a baryon overdensity $\delta = 10$ at the filament spine, and baryon density and temperature profiles following Tuominen *et al.* [41]’s results for massive filaments in the EAGLE simulation. We found

pressure and baryon density contributions of an importance similar to or lesser than that of the group, even at Mpc-scale distances. We thus considered the addition of the filament unnecessary, especially in light of model uncertainties such as the group's mass and the surmised validity of extrapolating the group's UPP to Mpc-scale distances.

We generated 21 evolutionary tracks of 200 time steps each, spanning a range jet powers $Q = 10^{38.8} - 10^{39.2}$ W. Propagating total length and radio luminosity uncertainties, we obtained $Q = 1.3 \pm 0.1 \cdot 10^{39}$ W and $T = 1.9_{-0.2}^{+0.7}$ Gyr. The outflow's jet power uncertainty is set by radio luminosity uncertainty while its age uncertainty is set by total length uncertainty. The inferred Gyr-scale age suggests that treating outflow evolution as a process at a single redshift — as is currently done in the model of Hardcastle [2] — is crude for the largest outflows, and may need revision. Each jet's average speed $\langle \beta \rangle := \frac{\langle v \rangle}{c} = \frac{l}{2cT} = 0.58_{-0.07}^{+0.04}\%$, where c is the speed of light. The energy transported by the jets $E = QT = 7.6_{-0.7}^{+2.1} \cdot 10^{55}$ J. As a black hole can redirect at most half of the rest energy of infalling matter to electromagnetic radiation and jet fuelling, and the energy an RE AGN spends on electromagnetic radiation must at least equal the energy spent on jet fuelling, the black hole must have gained a mass $\Delta M_{\bullet} > 2 \frac{E}{c^2} = 8.5_{-0.8}^{+2.4} \cdot 10^8 M_{\odot}$ while powering the jets.

Total outflow length To estimate Porphyryon's total length from its projected length, we perform statistical deprojection. Equation 9 of Oei *et al.* [42] stipulates the probability density function (PDF) of an outflow's total length random variable (RV) L in case its projected length RV L_p is known to equal some value l_p . This PDF is parametrised by the tail index ξ of the Pareto distribution assumed to describe L . We calculate the median and expectation value of $L | L_p = l_p$ for tail indices $\xi = -3$ and $\xi = -4$, the integer values closest to the observationally favoured $\xi = -3.5 \pm 0.5$ [42].

First, we determine the cumulative distribution function (CDF) of $L | L_p = l_p$ through integration:

$$\begin{aligned} F_{L|L_p=l_p}(l) &:= \int_{-\infty}^l f_{L|L_p=l_p}(l') dl' \\ &= \frac{-\xi}{2^{1+\xi}\pi} \frac{\Gamma^2(-\frac{\xi}{2})}{\Gamma(-\xi)} \int_1^{\max\{x,1\}} \frac{x'^{\xi-1}}{\sqrt{x'^2-1}} dx', \end{aligned} \quad (2)$$

where $x := \frac{l}{l_p}$ and $x' := \frac{l'}{l_p}$.

For $\xi = -3$, the CDF concretises to

$$F_{L|L_p=l_p}(l) = \frac{3}{2} \int_1^{\max\{x,1\}} \frac{dx'}{x'^4 \sqrt{x'^2 - 1}} \quad (3)$$

$$= \begin{cases} 0 & \text{if } x < 1; \\ \frac{(2x^2+1)\sqrt{x^2-1}}{2x^3} & \text{if } x \geq 1. \end{cases}$$

The median conditional total length, l_m , is defined by $F_{L|L_p=l_p}(l_m) := \frac{1}{2}$. Numerically, we obtain $x_m := \frac{l_m}{l_p} \approx 1.0664$, or $l_m \approx 1.0664 l_p$. As $l_p = 6.43 \pm 0.05$ Mpc, we find $l_m = 6.86 \pm 0.05$ Mpc. An analogous numerical determination of the 16-th and 84-th percentiles then yields $l = 6.9_{-0.4}^{+1.6}$ Mpc.

For $\xi = -4$, the CDF concretises to

$$F_{L|L_p=l_p}(l) = \frac{16}{3\pi} \int_1^{\max\{x,1\}} \frac{dx'}{x'^5 \sqrt{x'^2 - 1}} \quad (4)$$

$$= \begin{cases} 0 & \text{if } x < 1; \\ \frac{2}{3\pi} \left(\frac{(3x^2+2)\sqrt{x^2-1}}{x^4} + 3 \arccos \frac{1}{x} \right) & \text{if } x \geq 1. \end{cases}$$

Numerically, we obtain $x_m \approx 1.0515$, or $l_m \approx 1.0515 l_p$, and thus $l_m = 6.76 \pm 0.05$ Mpc. In the same way as before, we find $l = 6.8_{-0.3}^{+1.2}$ Mpc.

Equation 10 of Oei *et al.* [42] gives a closed-form expression for $\mathbb{E}[L | L_p = l_p](\xi)$. Table 1 of the same work lists $\mathbb{E}[L | L_p = l_p](\xi = -3) = \frac{3\pi}{8} l_p$ and $\mathbb{E}[L | L_p = l_p](\xi = -4) = \frac{32}{9\pi} l_p$. In the case of Porphyron, these expressions concretise to $\mathbb{E}[L | L_p = l_p](\xi = -3) = 7.58 \pm 0.06$ Mpc and $\mathbb{E}[L | L_p = l_p](\xi = -4) = 7.28 \pm 0.05$ Mpc.

By conditioning L on more knowledge than a value for L_p alone, statistical deprojection could be made more precise. For example, one could additionally condition on the fact that Porphyron is generated by a Type 2 radiatively efficient (RE) AGN. If Type 1 RE AGN are seen mostly face-on and Type 2 RE AGN are seen mostly edge-on, as proposed by the unification model [e.g. 43], then the detection of a Type 2 RE AGN would imply that the jets make a small angle with the sky plane. Extending the formulae to include this knowledge is beyond the scope of this work; however, mindful of the associated deprojection factor-reducing effect, we

563 choose $\xi = -4$ as our fiducial tail index.

564 To assess Porphyron's transport capabilities in a cosmological context, it is instructive to calculate its length
 565 relative to Cosmic Web length scales. In particular, the outflow's total length relative to the typical cosmic
 566 void radius at its epoch is $f_v := l(1+z)R_v^{-1}$, where R_v is the typical comoving cosmic void radius. For
 567 $l = 6.8_{-0.3}^{+1.2}$ Mpc, $z = 0.896 \pm 0.001$, and $R_v = 20$ Mpc [44], we find $f_v = 64_{-2}^{+12}$ %. For our fiducial total
 568 length $l = 7$ Mpc, we find $f_v = 66$ %.

569 **Filament shape modification** We predict that powerful, long-lived outflows like Porphyron cause their host
 570 galaxies' filaments to expand thermally. Through lateral shocks, the jets distribute an amount of heat Q_{WHIM}
 571 over the warm-hot IGM. This medium is sufficiently dilute that plasma interactions can be neglected; as a
 572 result, the ideal gas law, $pV = Nk_B T$, may be adopted as the equation of state. Here, p , V , N , and T are the
 573 filament's pressure, volume, plasma particle number, and temperature, respectively; k_B is Boltzmann's constant.
 574 Assuming a thermodynamic process at constant pressure and particle number, the work W is

$$W = p\Delta V = Nk_B\Delta T. \quad (5)$$

575 Before the outflow's emergence, the filament's equation of state is $pV_i = Nk_B T_i$, where V_i and T_i are its initial
 576 volume and temperature, respectively. Upon dividing Eq. 5 by this equation of state, one obtains

$$\frac{\Delta V}{V_i} = \frac{\Delta T}{T_i}. \quad (6)$$

577 Assuming that the filament retains a cylindrical shape, initially with radius r_i and finally with radius r_f , and
 578 using that $\Delta V := V_f - V_i$, one obtains

$$\frac{r_f}{r_i} = \sqrt{1 + \frac{\Delta T}{T_i}}. \quad (7)$$

579 The radius ratio, $\frac{r_f}{r_i}$, depends only on the ratio between the temperature increase $\Delta T := T_f - T_i$ and the initial
 580 temperature. The temperature increase is

$$\Delta T = \frac{Q_{\text{WHIM}}}{NC_{\text{p,m}}}, \quad (8)$$

581 where $C_{\text{p,m}}$ is the molar heat capacity at constant pressure. For a monatomic gas or a hydrogen plasma, $C_{\text{p,m}} =$
 582 $\frac{5}{2}R$, where R is the molar gas constant. The number of filamentary electrons and atomic nuclei affected by the
 583 outflow is

$$N = \frac{\pi r_i^2 L \rho_i}{\mu m_p}, \quad (9)$$

584 where L is the length of the cylindrical segment affected, ρ_i is the initial baryonic mass density, μ is the average
 585 mass of a plasma particle relative to the proton mass, and m_p is the proton mass. We estimate $\frac{L}{2}$ by multiplying
 586 the typical speed of lateral shocks with the outflow's lifetime. We decompose $\rho_i = \rho_{\text{c},0} \Omega_{\text{BM},0} (1+z)^3 (1+\delta)$,
 587 where z and δ are the filament's cosmological redshift and baryonic overdensity, respectively.

588 To estimate Q_{WHIM} given E , the total energy carried by the jets up to the time of observation, we turn to
 589 analytical models and numerical simulations. Modelling indicates that just $\sim 10\%$ of the total energy is lost
 590 through radiative processes [2]. This fraction increases with redshift, as inverse-Compton losses to the CMB
 591 become more pronounced. Numerical simulations show that, at least in galaxy clusters, $\sim 50\%$ of the non-
 592 radiated energy is converted into thermal or kinetic energy carried by the shocked medium, and the other $\sim 50\%$
 593 is converted into thermal or kinetic energy carried by the outflow's lobes [45]. Over time, the kinetic energy turns
 594 into thermal energy. It is, at present, unclear how fast remnant lobes mix with the surrounding medium, and
 595 how the mixing timescale varies with the latter's density. Here we assume that, at late times, all of the lobes'
 596 energy mixes with the surrounding medium. As such, we estimate $Q_{\text{WHIM}} \rightarrow 90\% \cdot E$.

597 We assess the outflow-induced morphological change to Porphyryon's filament by evaluating Eq. 7, taking
 598 $Q_{\text{WHIM}} = 7 \cdot 10^{55}$ J, $r_i \approx r_c = 1.2$ Mpc (a typical filament core radius [41]), $L = 2 \cdot 7$ Mpc = 14 Mpc
 599 (assuming that the region beyond the outflow's direct reach that is affected at late times is comparable in length
 600 to the outflow itself), $z = 0.9$, $1 + \delta = 10$, $\mu = 0.5$, and $T_i = 10^7$ K; we find $\Delta T = 3 \cdot 10^7$ K (an increase of

601 $\sim 300\%$) and $r_f = 2.4$ Mpc (an increase of $\sim 100\%$). Porphyrion's heat dissipation renders the outflow's native
602 filament much hotter and thicker than it would have otherwise been.

603 For our cosmological outlook, we assumed a typical jet power and age that are each an order of magni-
604 tude lower than Porphyrion's. We thus estimated the combined energy carried by 10 Mpc-scale outflows to be
605 $Q_{\text{WHIM}} = 7 \cdot 10^{54}$ J. Assuming non-overlapping affected regions, we estimated $L = 10 \cdot 2 \cdot 1$ Mpc = 20 Mpc.
606 Leaving all other parameters identical, we find $\Delta T = 2 \cdot 10^6$ K (an increase of $\sim 20\%$) and $r_f = 1.3$ Mpc (an
607 increase of $\sim 10\%$).

608 **Quasar mass–based host galaxy candidate elimination** SDSS J152933.03+601552.5 is the quasar-hosting
609 galaxy 19'' north-northeast of J152932.16+601534.4, the galaxy we have identified as Porphyrion's host. We ini-
610 tially also considered SDSS J152933.03+601552.5 as a host galaxy candidate. However, aforementioned arguments
611 involving the presence of jets and their orientation and, to a lesser degree, arguments involving core radio lumi-
612 nosity and core synchrotron self-absorption all favour J152932.16+601534.4. We now discuss how our results
613 would change if, instead, SDSS J152933.03+601552.5 were Porphyrion's host galaxy. Doing so will lead to a con-
614 tradiction that disproves this alternative hypothesis.

615 First, we discuss results that do not require dynamical modelling. To start with, Porphyrion would remain
616 generated by an RE AGN. The host galaxy redshift would decrease from $z = 0.896 \pm 0.001$ to $z = 0.799 \pm$
617 0.001 , decreasing Porphyrion's projected length from $l_p = 6.43 \pm 0.05$ Mpc to $l_p = 6.21 \pm 0.05$ Mpc. Again
618 using $\xi = -4$, the total length would decrease from $l = 6.8_{-0.3}^{+1.2}$ Mpc to $l = 6.5_{-0.3}^{+1.2}$ Mpc and its conditional
619 expectation from $\mathbb{E}[L \mid L_p = l_p] = 7.28 \pm 0.05$ Mpc to $\mathbb{E}[L \mid L_p = l_p] = 7.03 \pm 0.06$ Mpc. If orientation
620 distinguishes Type 1 from Type 2 RE AGN, as the unification model supposes, then these statistical deprojection
621 results may underestimate Porphyrion's total length. Porphyrion would remain the projectively longest galaxy-
622 made structure identified so far. The host's stellar mass would decrease from $M_\star = 6.7 \pm 1.4 \cdot 10^{11} M_\odot$ to
623 $M_\star = 4.0_{-0.3}^{+0.3} \cdot 10^{11} M_\odot$, while the SFR would become $S = 4.9_{-0.4}^{+0.3} \cdot 10^1 M_\odot \text{ yr}^{-1}$ [46]. Porphyrion's total
624 radio luminosity at rest-frame wavelength $\lambda_r = 2$ m would decrease from $L_\nu = 2.8 \pm 0.3 \cdot 10^{26} \text{ W Hz}^{-1}$ to
625 $L_\nu = 2.2 \pm 0.2 \cdot 10^{26} \text{ W Hz}^{-1}$.

626 Next, we discuss results that come from dynamical modelling. The jet power would decrease from $Q =$
627 $1.3 \pm 0.1 \cdot 10^{39} \text{ W}$ to $Q = 1.0 \pm 0.1 \cdot 10^{39} \text{ W}$, while the age would slightly increase from $T = 1.9_{-0.2}^{+0.7} \text{ Gyr}$ to

$T = 1.9^{+0.7}_{-0.1}$ Gyr. The transported energy would decrease from $E = 7.6^{+2.1}_{-0.7} \cdot 10^{55}$ J to $E = 6.4^{+1.8}_{-0.6} \cdot 10^{55}$ J, and the minimum black hole mass gain from $\Delta M_{\bullet} > 8.5^{+2.4}_{-0.8} \cdot 10^8 M_{\odot}$ to $\Delta M_{\bullet} > 7.2^{+2.0}_{-0.7} \cdot 10^8 M_{\odot}$.

Finally, we arrive at a contradiction, as the quasar’s SMBH mass (measured from its SDSS BOSS spectrum) $M_{\bullet} = 2.5 \pm 0.3 \cdot 10^8 M_{\odot}$ [47]. This mass is lower than the minimum mass gain associated to the fuelling of Porphyrior’s jets. Thus, assuming that SDSS J152933.03+601552.5 is the outflow’s host galaxy leads to a contradiction. This argument reaffirms that J152932.16+601534.4 is Porphyrior’s host.

Data availability The LoTSS DR2 is publicly available [48]. The authors share this work’s proprietary LOFAR, uGMRT, and Keck I Telescope data, as well as the dynamical model runs and LoTSS–VLASS spectral indices, through Code Ocean.

Code availability The dynamical model used to interpret the outflow is described by Hardcastle [2] and available for download [49]. Analysis and plotting code specific to this work is available on Code Ocean [50]. There are no access restrictions.

References

1. Planck Collaboration *et al.* Planck 2018 results. VI. Cosmological parameters. *Astron. Astrophys.* **641**, A6 (2020).
2. Hardcastle, M. J. A simulation-based analytic model of radio galaxies. *Mon. Not. R. Astron. Soc.* **475**, 2768–2786 (2018).
3. van Haarlem, M. P. *et al.* LOFAR: The LOw-Frequency ARray. *Astron. Astrophys.* **556**, A2 (2013).
4. Shimwell, T. W. *et al.* The LOFAR Two-metre Sky Survey. V. Second data release. *Astron. Astrophys.* **659**, A1 (2022).
5. Shimwell, T. W. *et al.* The LOFAR Two-metre Sky Survey. I. Survey description and preliminary data release. *Astron. Astrophys.* **598**, A104 (2017).
6. Tasse, C. *et al.* *DDFacet: Facet-based radio imaging package* Astrophysics Source Code Library, record ascl:2305.008. 2023.
7. van Weeren, R. J. *et al.* LOFAR observations of galaxy clusters in HETDEX. Extraction and self-calibration of individual LOFAR targets. *Astron. Astrophys.* **651**, A115 (2021).
8. Offringa, A. R. *et al.* WSCLEAN: an implementation of a fast, generic wide-field imager for radio astronomy. *Mon. Not. R. Astron. Soc.* **444**, 606–619 (2014).

9. Morabito, L. K. *et al.* Sub-arcsecond imaging with the International LOFAR Telescope. I. Foundational calibration strategy and pipeline. *Astron. Astrophys.* **658**, A1 (2022).
10. Jackson, N. *et al.* LBCS: The LOFAR Long-Baseline Calibrator Survey. *Astron. Astrophys.* **595**, A86 (2016).
11. Jackson, N. *et al.* Sub-arcsecond imaging with the International LOFAR Telescope. II. Completion of the LOFAR Long-Baseline Calibrator Survey. *Astron. Astrophys.* **658**, A2 (2022).
12. Gupta, Y. *et al.* The upgraded GMRT: opening new windows on the radio Universe. *Current Science* **113**, 707–714 (2017).
13. Intema, H. T. *SPAM: Source Peeling and Atmospheric Modeling* Astrophysics Source Code Library, record ascl:1408.006. 2014.
14. Mohan, N. & Rafferty, D. *PyBDSF: Python Blob Detection and Source Finder* Astrophysics Source Code Library, record ascl:1502.007. 2015.
15. Blandford, R. D. & Znajek, R. L. Electromagnetic extraction of energy from Kerr black holes. *Mon. Not. R. Astron. Soc.* **179**, 433–456 (1977).
16. Hardcastle, M. J. *et al.* Radio-loud AGN in the first LoTSS data release. The lifetimes and environmental impact of jet-driven sources. *Astron. Astrophys.* **622**, A12 (2019).
17. Alam, S. *et al.* The Eleventh and Twelfth Data Releases of the Sloan Digital Sky Survey: Final Data from SDSS-III. *Astrophys. J. Sup.* **219**, 12 (2015).
18. Dey, A. *et al.* Overview of the DESI Legacy Imaging Surveys. *Astron. J.* **157**, 168 (2019).
19. Duncan, K. J. All-purpose, all-sky photometric redshifts for the Legacy Imaging Surveys Data Release 8. *Mon. Not. R. Astron. Soc.* **512**, 3662–3683 (2022).
20. Oke, J. B. *et al.* The Keck Low-Resolution Imaging Spectrometer. *PASP* **107**, 375 (1995).
21. McCarthy, J. K. *et al.* *Blue channel of the Keck low-resolution imaging spectrometer* in *Optical Astronomical Instrumentation* (ed D’Odorico, S.) **3355** (1998), 81–92.
22. Steidel, C. C. *et al.* A Survey of Star-forming Galaxies in the $1.4 \lesssim z \lesssim 2.5$ Redshift Desert: Overview. *Astrophys. J.* **604**, 534–550 (2004).
23. Rockosi, C. *et al.* *The low-resolution imaging spectrograph red channel CCD upgrade: fully depleted, high-resistivity CCDs for Keck* in *Ground-based and Airborne Instrumentation for Astronomy III* (eds McLean, I. S., Ramsay, S. K. & Takami, H.) **7735** (2010), 77350R.
24. Prochaska, J. *et al.* PypeIt: The Python Spectroscopic Data Reduction Pipeline. *The Journal of Open Source Software* **5**, 2308 (2020).
25. Dawson, K. S. *et al.* The Baryon Oscillation Spectroscopic Survey of SDSS-III. *Astron. J.* **145**, 10 (2013).

- 681 26. Chambers, K. C. *et al.* The Pan-STARRS1 Surveys. *arXiv e-prints*, arXiv:1612.05560 (2016).
- 682 27. Jarrett, T. H. *et al.* The Spitzer-WISE Survey of the Ecliptic Poles. *Astrophys. J.* **735**, 112 (2011).
- 683 28. Calistro Rivera, G., Lusso, E., Hennawi, J. F. & Hogg, D. W. AGNfitter: A Bayesian MCMC Approach to Fitting Spectral
684 Energy Distributions of AGNs. *Astrophys. J.* **833**, 98 (2016).
- 685 29. Martínez-Ramírez, L. N. *et al.* AGNfitter-rx: Modelling the radio-to-X-ray SEDs of AGNs. *arXiv e-prints*, arXiv:2405.12111
686 (2024).
- 687 30. Hardcastle, M. J. *et al.* The LOFAR Two-Metre Sky Survey. VI. Optical identifications for the second data release. *Astron.*
688 *Astrophys.* **678**, A151 (2023).
- 689 31. Mostert, R. I. J. *et al.* Constraining the giant radio galaxy population with machine learning and Bayesian inference. *arXiv*
690 *e-prints*, arXiv:2405.00232 (2024).
- 691 32. Oei, M. S. S. L. *et al.* Luminous giants populate the dense Cosmic Web: The radio luminosity-environmental density relation
692 for radio galaxies in action. *arXiv e-prints*, arXiv:2404.17776 (2024).
- 693 33. Wen, Z. L. & Han, J. L. A catalog of 1.58 million clusters of galaxies identified from the DESI Legacy Imaging Surveys. *arXiv*
694 *e-prints*, arXiv:2404.02002 (2024).
- 695 34. Pasini, T. *et al.* Radio galaxies in galaxy groups: kinematics, scaling relations, and AGN feedback. *Mon. Not. R. Astron. Soc.*
696 **505**, 2628–2637 (2021).
- 697 35. Arnaud, M. *et al.* The universal galaxy cluster pressure profile from a representative sample of nearby systems (REXCESS) and
698 the $Y_{SZ} - M_{500}$ relation. *Astron. Astrophys.* **517**, A92 (2010).
- 699 36. Sun, M. *et al.* The Pressure Profiles of Hot Gas in Local Galaxy Groups. *Astrophys. J. Let.* **727**, L49 (2011).
- 700 37. Cooke, R. J. & Fumagalli, M. Measurement of the primordial helium abundance from the intergalactic medium. *Nature As-*
701 *tronomy* **2**, 957–961 (2018).
- 702 38. Lovisari, L., Reiprich, T. H. & Schellenberger, G. Scaling properties of a complete X-ray selected galaxy group sample. *Astron.*
703 *Astrophys.* **573**, A118 (2015).
- 704 39. Ricciardelli, E., Quilis, V. & Planelles, S. The structure of cosmic voids in a Λ CDM Universe. *Mon. Not. R. Astron. Soc.* **434**,
705 1192–1204 (2013).
- 706 40. Upton Sanderbeck, P. R., D’Aloisio, A. & McQuinn, M. J. Models of the thermal evolution of the intergalactic medium after
707 reionization. *Mon. Not. R. Astron. Soc.* **460**, 1885–1897 (2016).
- 708 41. Tuominen, T. *et al.* An EAGLE view of the missing baryons. *Astron. Astrophys.* **646**, A156 (2021).
- 709 42. Oei, M. S. S. L. *et al.* Measuring the giant radio galaxy length distribution with the LoTSS. *Astron. Astrophys.* **672**, A163 (2023).

- 710 43. Heckman, T. M. & Best, P. N. The Coevolution of Galaxies and Supermassive Black Holes: Insights from Surveys of the Con-
711 temporary Universe. *ARA&A* **52**, 589–660 (2014).
- 712 44. Correa, C. M. *et al.* Redshift-space effects in voids and their impact on cosmological tests. Part I: the void size function. *Mon.*
713 *Not. R. Astron. Soc.* **500**, 911–925 (2021).
- 714 45. Hardcastle, M. J. & Krause, M. G. H. Numerical modelling of the lobes of radio galaxies in cluster environments. *Mon. Not.*
715 *R. Astron. Soc.* **430**, 174–196 (2013).
- 716 46. Barrows, R. S., Comerford, J. M., Stern, D. & Assef, R. J. A Catalog of Host Galaxies for WISE-selected AGN: Connecting
717 Host Properties with Nuclear Activity and Identifying Contaminants. *Astrophys. J.* **922**, 179 (2021).
- 718 47. Chen, Z.-F., Pan, D.-S., Pang, T.-T. & Huang, Y. A Catalog of Quasar Properties from the Baryon Oscillation Spectroscopic
719 Survey. *Astrophys. J. Sup.* **234**, 16 (2018).
- 720 48. LOFAR Collaboration. Website for LOFAR surveys data, including LoTSS DR2. 2022. <https://lofar-surveys.org>.
- 721 49. Hardcastle, M. J. GitHub repository for ‘A simulation-based analytic model of radio galaxies’. 2021. [https://github.com/](https://github.com/mhardcastle/analytic)
722 [mhardcastle/analytic](https://github.com/mhardcastle/analytic).
- 723 50. Oei, M. S. S. L. Code Ocean capsule for ‘Black hole jets on the scale of the Cosmic Web’. 2024. [https://codeocean.com/](https://codeocean.com/capsule/3908804/tree)
724 [capsule/3908804/tree](https://codeocean.com/capsule/3908804/tree).
- 725 51. Sweijen, F. GitHub repository for legacystamps. 2021. <https://github.com/tikk3r/legacystamps>.
- 726 52. Lang, D., Hogg, D. W. & Schlegel, D. J. WISE Photometry for 400 Million SDSS Sources. *Astron. J.* **151**, 36 (2016).
- 727 53. Gordon, Y. A. *et al.* A Quick Look at the 3 GHz Radio Sky. I. Source Statistics from the Very Large Array Sky Survey. *Astrophys.*
728 *J. Sup.* **255**, 30 (2021).
- 729 54. Helfand, D. J., White, R. L. & Becker, R. H. The Last of FIRST: The Final Catalog and Source Identifications. *Astrophys. J.*
730 **801**, 26 (2015).

731 **Acknowledgments** M.S.S.L.O. and R.J.v.W. acknowledge support from the VIDI research programme with
732 project number 639.042.729, which is financed by the Dutch Research Council (NWO). M.S.S.L.O. also ac-
733 knowledges support from the CAS–NWO programme for radio astronomy with project number 629.001.024,
734 which is financed by the NWO. In addition, M.S.S.L.O., R.T., and R.J.v.W. acknowledge support from the ERC
735 Starting Grant ClusterWeb 804208. M.J.H. acknowledges support from the UK STFC [ST/V000624/1]. R.T.
736 is grateful for support from the UKRI Future Leaders Fellowship (grant MR/To42842/1). A.B. acknowledges
737 financial support from the European Union - Next Generation EU. F.d.G. acknowledges support from the

738 ERC Consolidator Grant ULU 101086378. The work of D.S. was carried out at the Jet Propulsion Laboratory,
 739 California Institute of Technology, under a contract with NASA. We thank Frits Sweijen for making available
 740 legacystamps [51]. We thank Riccardo Caniato for illuminating discussions. LOFAR data products were
 741 provided by the LOFAR Surveys Key Science project (LSKSP; [48]) and were derived from observations with
 742 the International LOFAR Telescope (ILT). LOFAR [3] is the Low Frequency Array designed and constructed
 743 by ASTRON. It has observing, data processing, and data storage facilities in several countries, which are owned
 744 by various parties (each with their own funding sources), and which are collectively operated by the ILT foun-
 745 dation under a joint scientific policy. The efforts of the LSKSP have benefited from funding from the European
 746 Research Council, NOVA, NWO, CNRS-INSU, the SURF Co-operative, the UK Science and Technology
 747 Funding Council, and the Jülich Supercomputing Centre. We thank the staff of the GMRT that made these
 748 observations possible. The GMRT is run by the National Centre for Radio Astrophysics of the Tata Institute
 749 of Fundamental Research. Some of the data presented herein were obtained at the W. M. Keck Observatory,
 750 which is operated as a scientific partnership among the California Institute of Technology, the University of
 751 California, and the National Aeronautics and Space Administration. The Observatory was made possible by
 752 the generous financial support of the W. M. Keck Foundation.

753 **Author contributions** A.R.D.J.G.I.B.G. and M.S.S.L.O. discovered Porphyryion; M.J.H., assisted by citizen
 754 scientists, independently found the outflow as part of LOFAR Galaxy Zoo. M.S.S.L.O. coordinated the ensuing
 755 project. R.J.v.W., H.J.A.R., and M.J.H. advised M.S.S.L.O. throughout. A.B. re-reduced and imaged the 6.2''
 756 and 19.8'' LOFAR data; R.J.v.W. contributed. R.T. reduced and imaged the 0.4'' LOFAR data. F.d.G. explored
 757 the use of LOFAR LBA data, which he reduced and imaged. M.S.S.L.O. wrote the uGMRT follow-up proposal.
 758 M.S.S.L.O. and H.T.I. reduced and imaged the uGMRT data. S.G.D., D.S., and H.J.A.R. were instrumental
 759 in securing Keck time (P.I.: S.G.D.). A.C.R. observed the host galaxy with LRIS; A.C.R. and D.S. reduced the
 760 data. G.C.R. determined the host galaxy's SED and stellar mass; M.S.S.L.O. contributed. M.J.H. determined
 761 core spectral indices of Mpc-scale outflows. M.S.S.L.O. determined the spurious association probability, the
 762 nearest galaxy cluster, and the circumgalactic Cosmic Web percentile. M.J.H. performed dynamical modelling;
 763 M.S.S.L.O. contributed. M.S.S.L.O. derived the deprojection and filament heating formulae. M.S.S.L.O. wrote
 764 the article, with contributions from A.R.D.J.G.I.B.G., R.T., and A.C.R. All authors provided comments to

765 improve the text.

766 **Author information** The authors declare no competing interests. Correspondence should be addressed to
767 Martijn S.S.L. Oei, who can be reached via e-mail: `oei@caltech.edu` or
768 `oei@strw.leidenuniv.nl`.

769 **Inclusion & ethics** We recognise that the Keck I Telescope observations on which this work relies have been
770 conducted from Maunakea, a site of high cultural and environmental significance for the Hawaiian people. We
771 are grateful for the opportunity to collect data here, and we support deepening astronomy’s commitment to
772 good stewardship of the mountain.

773 Extended Data Figure legends

- 774 1 **ILT image of Porphyrior at a lower resolution of 19.8''**. The image, again at central wave-
775 length $\lambda = 2.08$ m, highlights diffuse emission in the northern lobe and southern backflow.
776 We show the same sky region and annotations as in Fig. 1. The contours denote significance at
777 fixed multiples of the image noise s.d. (σ): 3σ , 5σ , and 10σ 38
- 778 2 **VLBI close-up of Porphyrior’s centre**. Our ILT image of Porphyrior’s central $3.84' \times 3.84'$
779 at $\lambda = 2.08$ m and $0.4''$ resolution covers a third of the total jet system and reveals two radio-
780 luminous AGN, detected at a significance of $\sim 40\sigma$ (s.d.). We overlay the overarching jet axis
781 (translucent white), determined from the northern lobe and southern hotspot (not shown), to
782 scale for a jet radius of 1 kpc. The jet axis appears to pass through J152932.16+601534.4. 39
- 783 3 **Rest-frame ultraviolet–optical spectroscopy of J152933.03+601552.5**. (This is the quasar-
784 hosting galaxy $19''$ north-northeast of Porphyrior’s host galaxy.) We identify redshifted hy-
785 drogen, carbon, oxygen, neon, and magnesium lines, jointly implying $z_s = 0.799 \pm 0.001$.
786 Forbidden lines from the quasar’s narrow-line region are shown in red. The spectrum has been
787 measured with the LRIS on the W. M. Keck Observatory’s Keck I Telescope. 40

4	Astrometric offsets for Porphyrion’s host galaxy. All flux densities used in the inference of the host galaxy SED occur within an arcsecond of the Legacy DR10–identified host position. Coloured disks show 1σ (s.d.) astrometric uncertainties, while grey circles denote angular distances from the Legacy DR10–identified host position. The golden stars mark all other Legacy DR10–identified sources in the angular vicinity of Porphyrion’s host.	41
5	Radio spectral indices around Porphyrion’s centre and southern tip. The top panel, which covers $3' \times 3'$, reveals synchrotron self-absorption at metre wavelengths in the host galaxy, consistent with the fuelling of powerful jets. The bottom panel, which covers $2' \times 2'$, reveals a hotspot with backflow. We show effective spectral indices α between 0.46–2.08 m, at a resolution of $6.2''$. From light to dark, the contours denote thermal noise–induced spectral index uncertainties (s.d.) of 0.05, 0.1, 0.2, and 0.3.	42
6	Radio spectral index distributions of the cores of Mpc-scale outflows. Using LoTSS and VLASS data, we determined 924 effective spectral indices α between 0.1–2.08 m. In grey, we indicate the bins in which the core spectral indices of J152932.16+601534.4, Porphyrion’s claimed host galaxy, and J152933.03+601552.5 fall. The distribution suggests that the spectral index of J152932.16+601534.4 ($\alpha = -0.18 \pm 0.06$) is more typical of Mpc-scale outflows than the spectral index of J152933.03+601552.5. (For J152933.03+601552.5, due to a VLASS non-detection, we show the LoTSS–uGMRT Band 4 spectral index.) The inset shows the same data as a function of redshift z . The golden subsample comprises Mpc-scale outflows whose redshifts differ at most $\Delta z = 0.1$ from those of either J152932.16+601534.4 or J152933.03+601552.5.	43
7	Probabilistic analysis of the distance to the nearest cluster. DESI Legacy Imaging Surveys DR10 galaxy cluster redshift uncertainties induce multimodal, asymmetric probability distributions over measures of distance between Porphyrion’s host galaxy and the nearest galaxy cluster. We mark median-centred intervals containing 68% and 95% of all probability. The data suggest that Porphyrion does not originate from a cluster.	44

813	8	Environmental profiles assumed in our dynamical modelling.	We show the pressure,
814			baryon density, and temperature external to the outflow as a function of proper (rather than
815			comoving) distance from Porphyrior’s AGN. The profiles consist of contributions from the
816			outflow’s presumed galaxy group and the adjacent voids. 45

817 **Extended Data Table legends**

818	1	Flux densities F_ν of Porphyrior’s host galaxy.	These are as measured, and thus have not
819			been corrected for Galactic extinction. To allow the reader to do so, we provide estimated
820			Galactic transmission fractions f_t . The uncertainties denote 1σ (s.d.). Entries are sorted by
821			the central wavelengths λ of the observing bands, which cover the electromagnetic spectrum
822			from the optical to the radio. ¹ 46

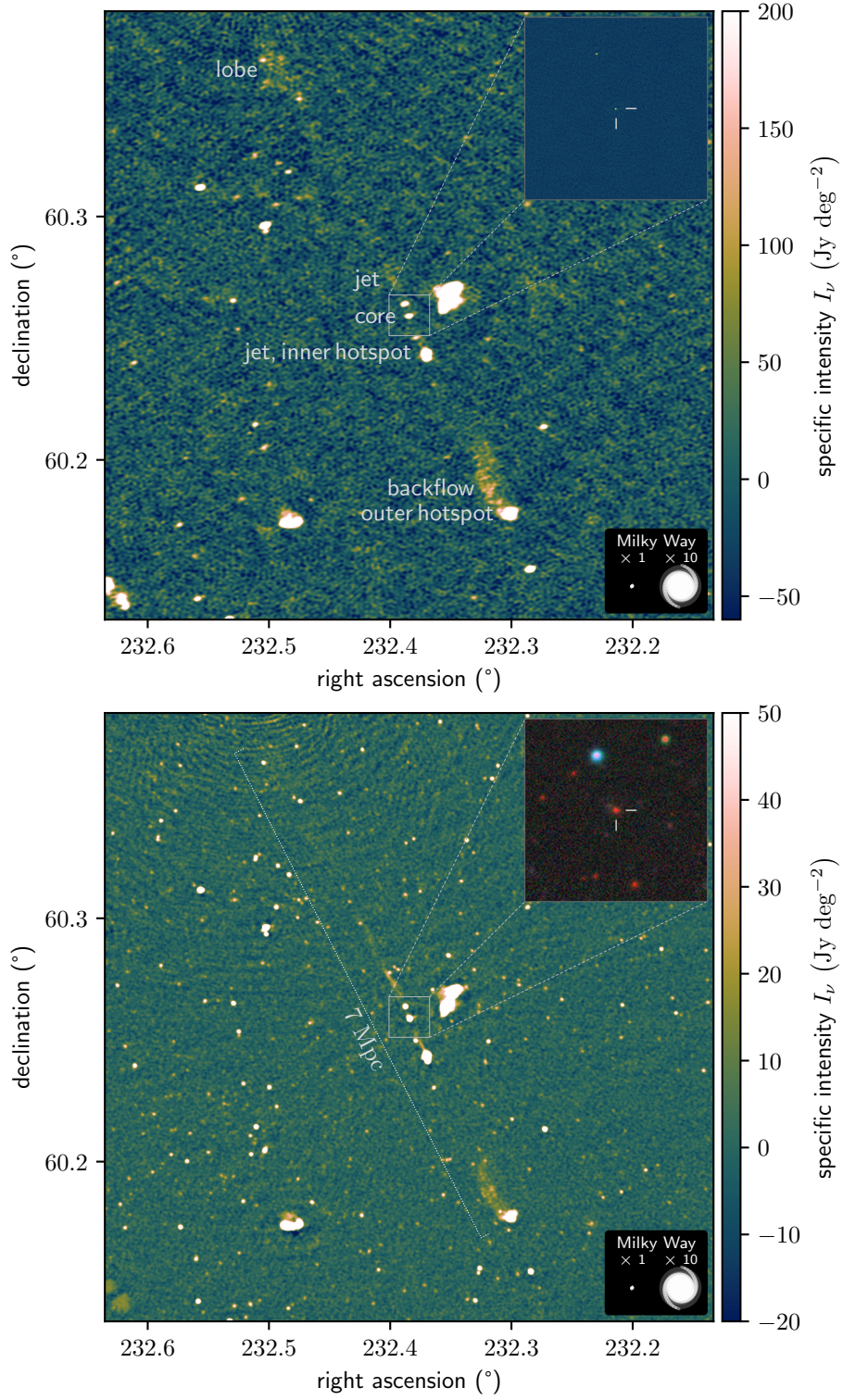


Figure 1: **Deep radio images of a 7 Mpc-long, black hole-driven outflow.** These images, (a) and (b), were taken with the ILT and uGMRT at central wavelengths $\lambda = 2.08$ m and $\lambda = 0.46$ m, respectively, and have resolutions of $6.2''$ and $4.3''$. Panel (a)'s inset shows ILT VLBI imagery at $\lambda = 2.08$ m and a resolution of $0.4''$. Panel (b)'s inset shows Legacy DR10 optical-infrared imagery. The larger images cover $15' \times 15'$ of sky, whilst the insets cover $1' \times 1'$. For scale, we show the stellar Milky Way disk (diameter: 50 kpc) and a ten times inflated version.

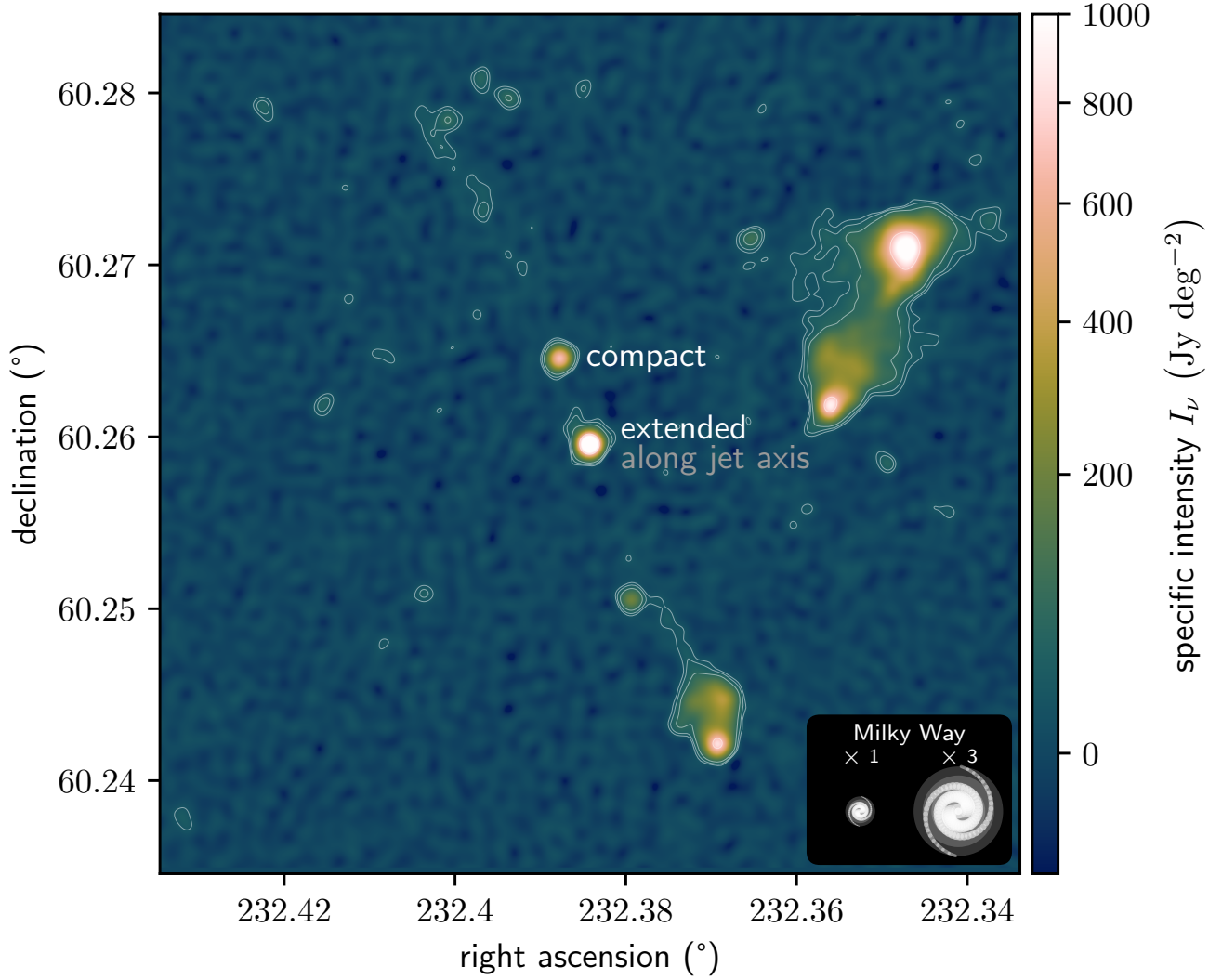


Figure 2: **Radio close-up of Porphyrion's centre.** In our imagery, only the southern host galaxy candidate features an extension along the outflow's overarching jet axis. For the central $3' \times 3'$ sky area, we show a uGMRT image at $\lambda = 0.46$ m and $3.6''$ resolution. We detect the southern galaxy's radio extension, directed towards the north-northeast, at 5 s.d. (σ) significance. The contours denote 3σ , 5σ , 10σ , and 100σ .

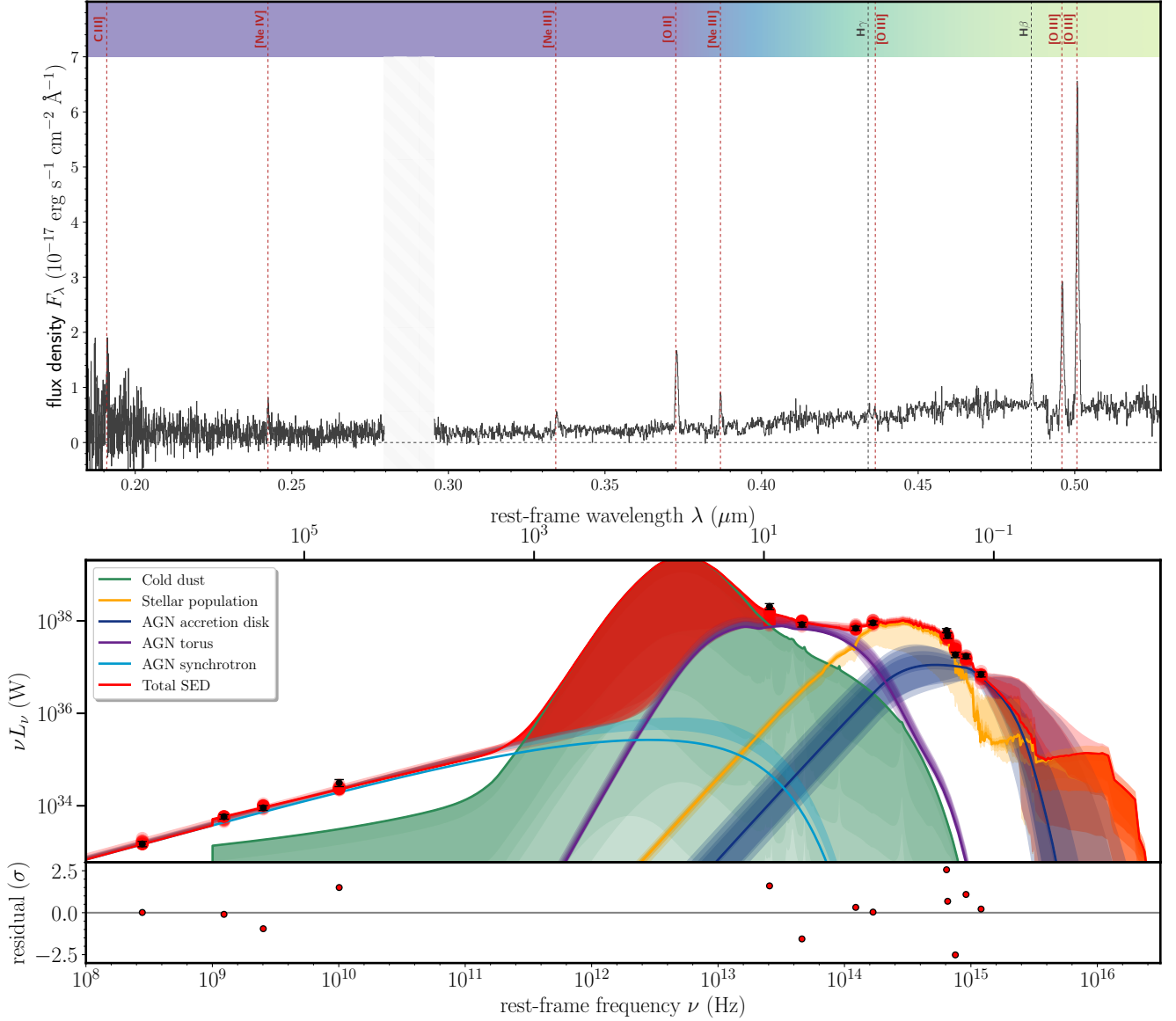


Figure 3: **Rest-frame ultraviolet–optical spectroscopy and radio–ultraviolet photometry of the host galaxy.** Both demonstrate that Porphyrios arises from an RE AGN. **a)** LRIS spectrum exhibiting hydrogen, carbon, oxygen, and neon emission. The forbidden lines from multiply ionised oxygen and neon (dark red) could not be generated by even the hottest stars, and instead stem from the narrow-line region of an RE AGN at a redshift $z = 0.896 \pm 0.001$. **b)** Bayesian inference of the galaxy’s SED (Methods) favours the presence of an AGN accretion disk (dark blue) with an obscuring torus (purple), again indicating radiative efficiency. Residuals are given in multiples of the s.d. (σ).

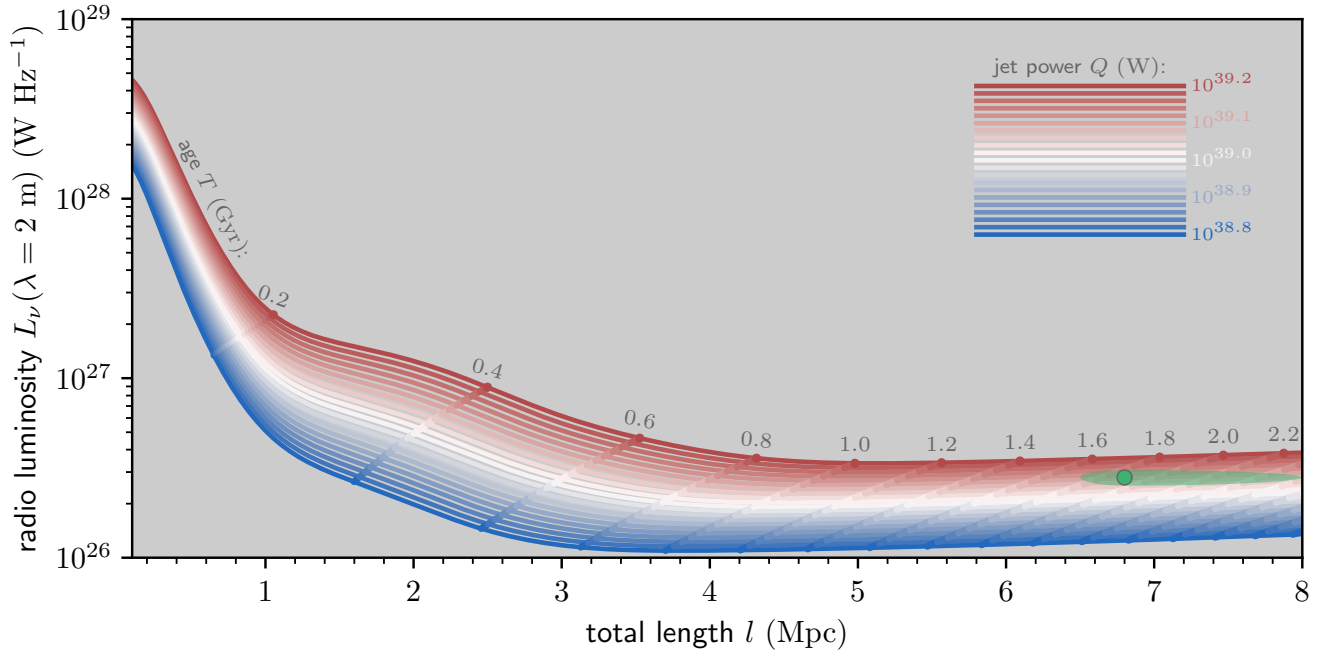
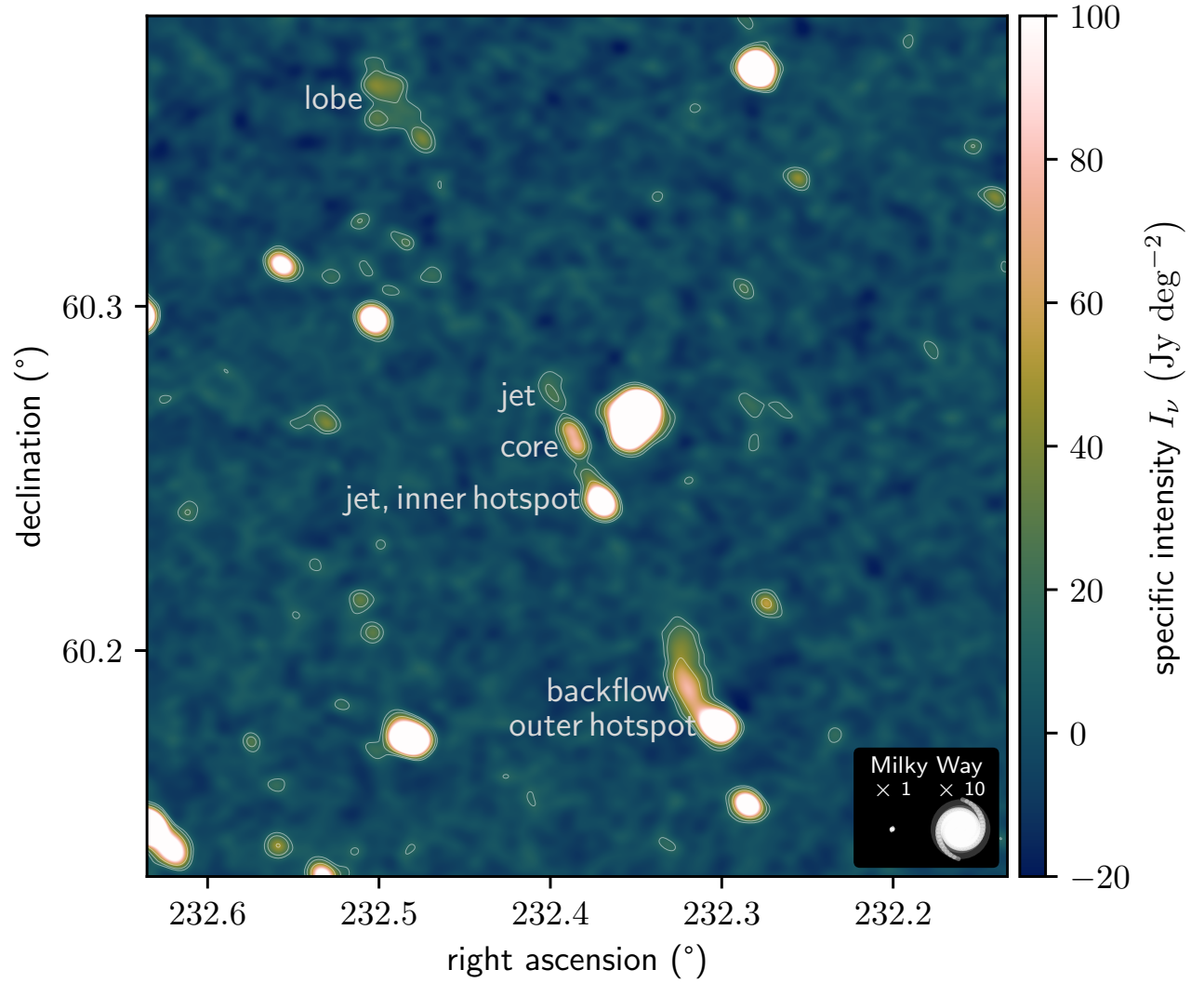
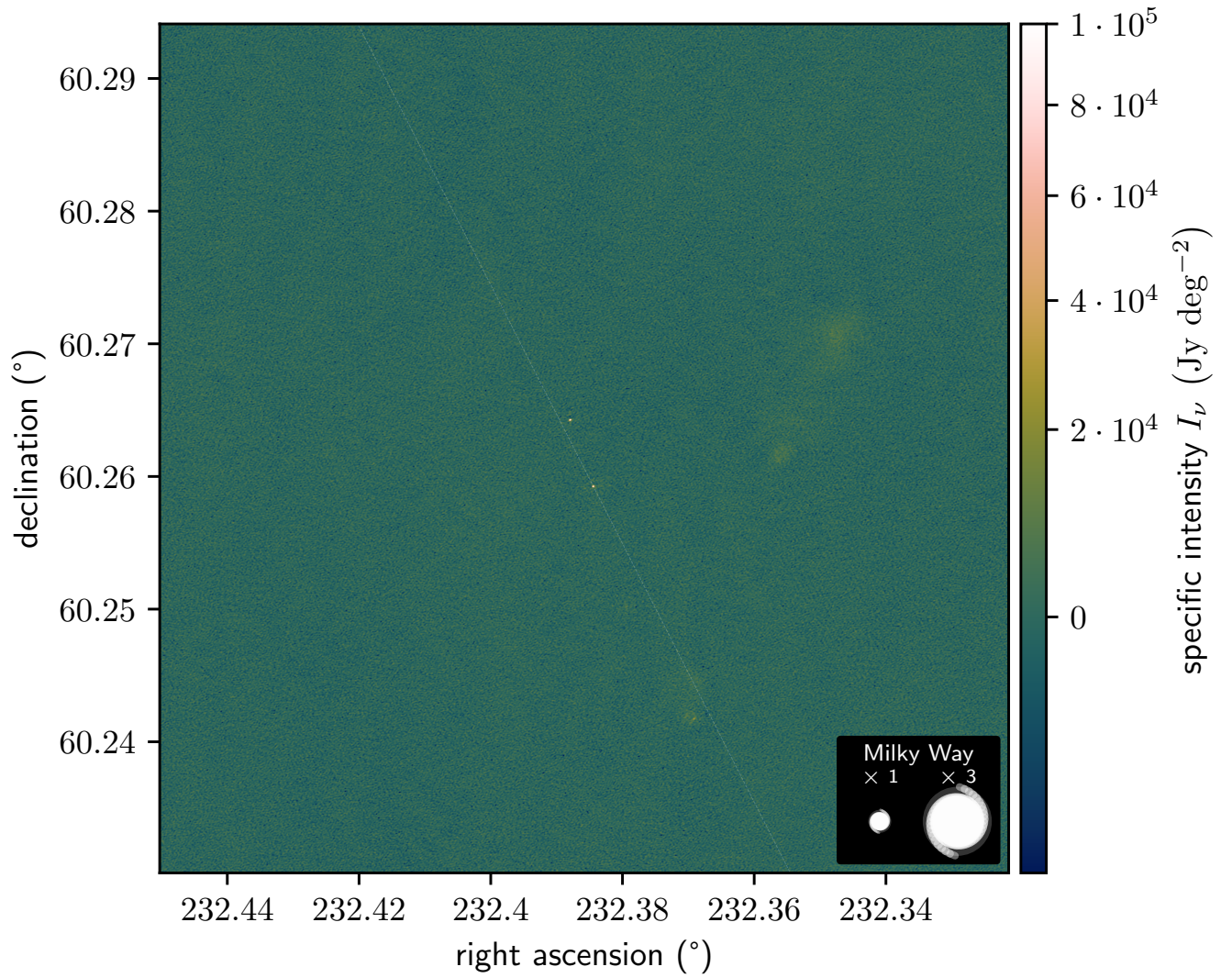


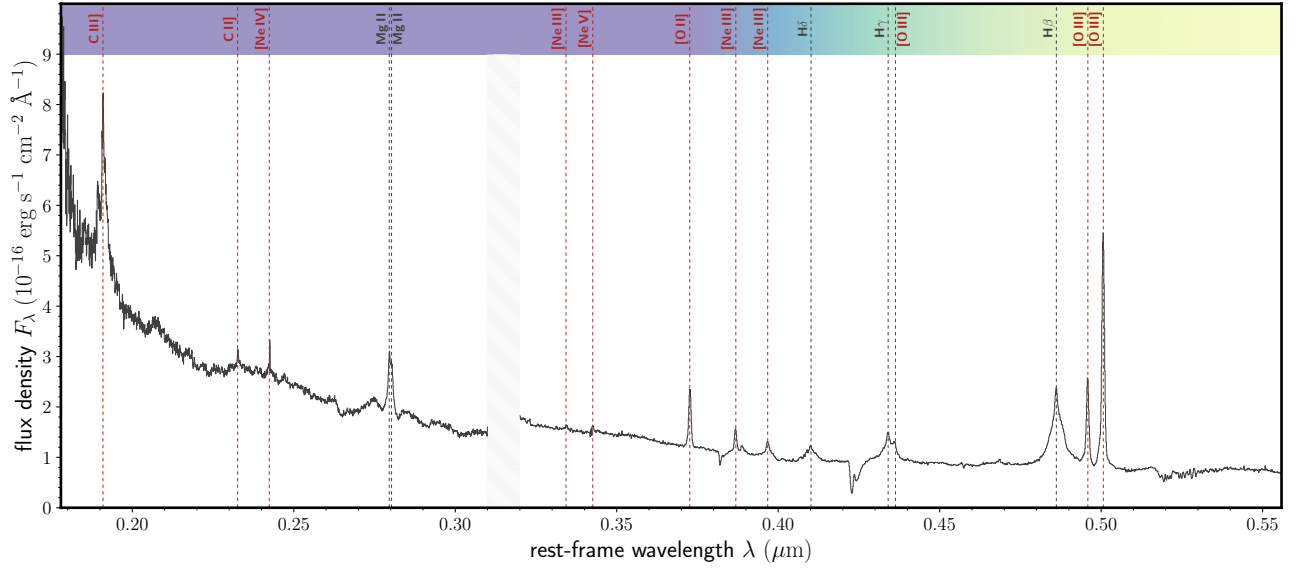
Figure 4: **Measurements overlaid on evolutionary tracks from dynamical modelling.** By superimposing Porphyrior's total length and radio luminosity on these tracks, we inferred the outflow's two-sided jet power and age. We assumed the host galaxy to reside in a galaxy group bordering voids, through which the jets eventually travel. The width and height of Porphyrior's uncertainty ellipse both cover 68% of probability centred around the median (green dot).



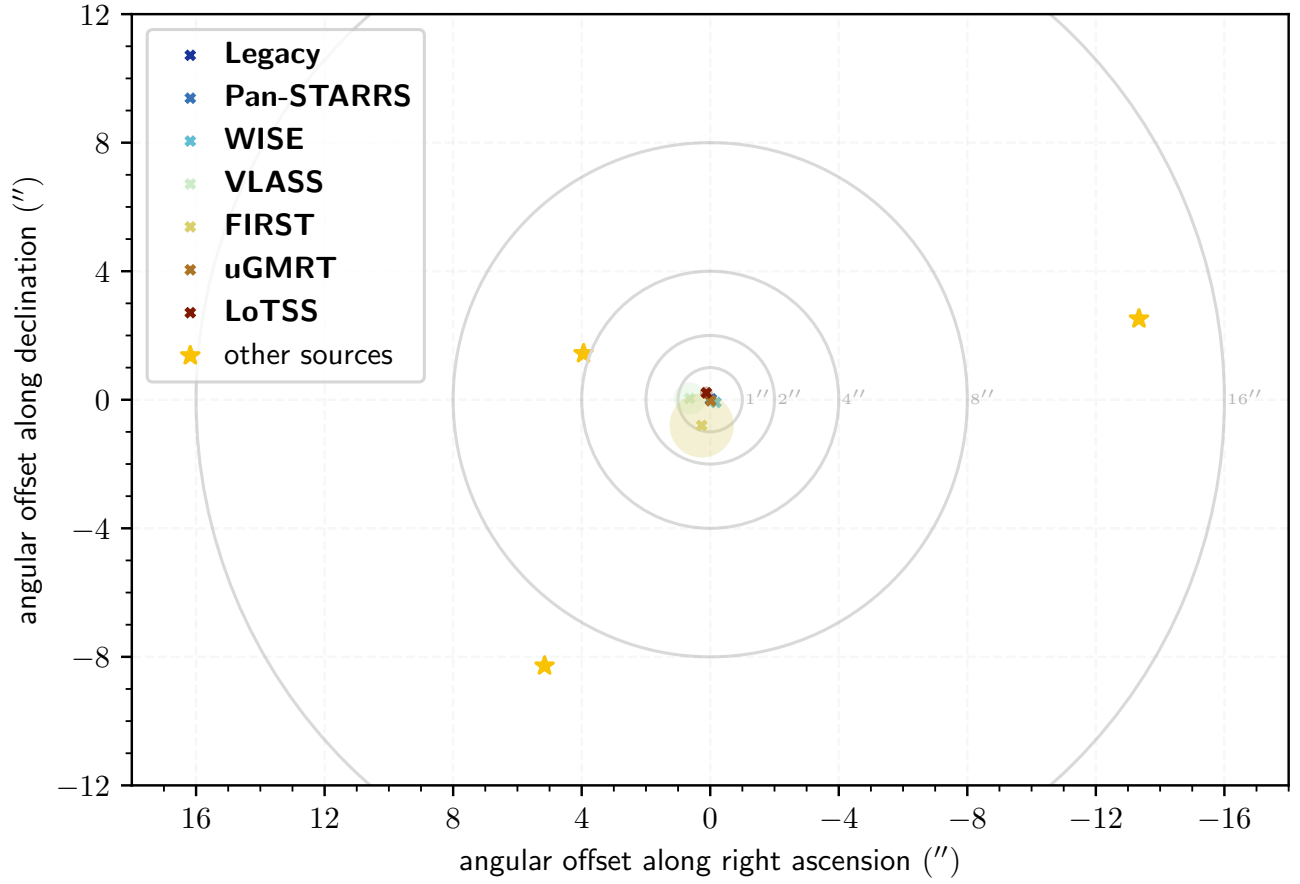
Extended Data Figure 1: **ILT image of Porphyrion at a lower resolution of $19.8''$** . The image, again at central wavelength $\lambda = 2.08$ m, highlights diffuse emission in the northern lobe and southern backflow. We show the same sky region and annotations as in Fig. 1. The contours denote significance at fixed multiples of the image noise s.d. (σ): 3σ , 5σ , and 10σ .



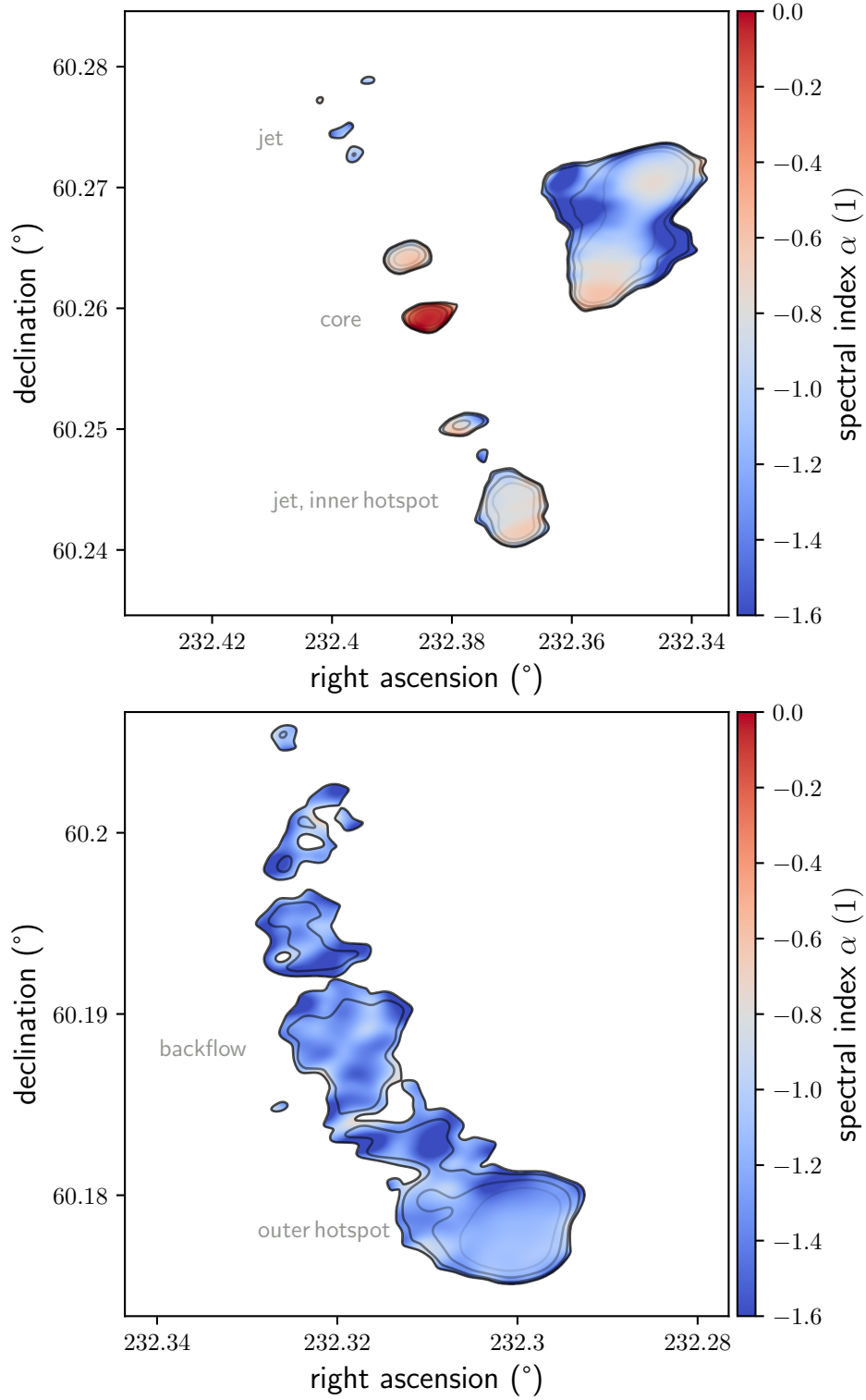
Extended Data Figure 2: **VLBI close-up of Porphyrion's centre.** Our ILT image of Porphyrion's central $3.84' \times 3.84'$ at $\lambda = 2.08$ m and $0.4''$ resolution covers a third of the total jet system and reveals two radio-luminous AGN, detected at a significance of $\sim 40\sigma$ (s.d.). We overlay the overarching jet axis (translucent white), determined from the northern lobe and southern hotspot (not shown), to scale for a jet radius of 1 kpc. The jet axis appears to pass through J152932.16+601534.4.



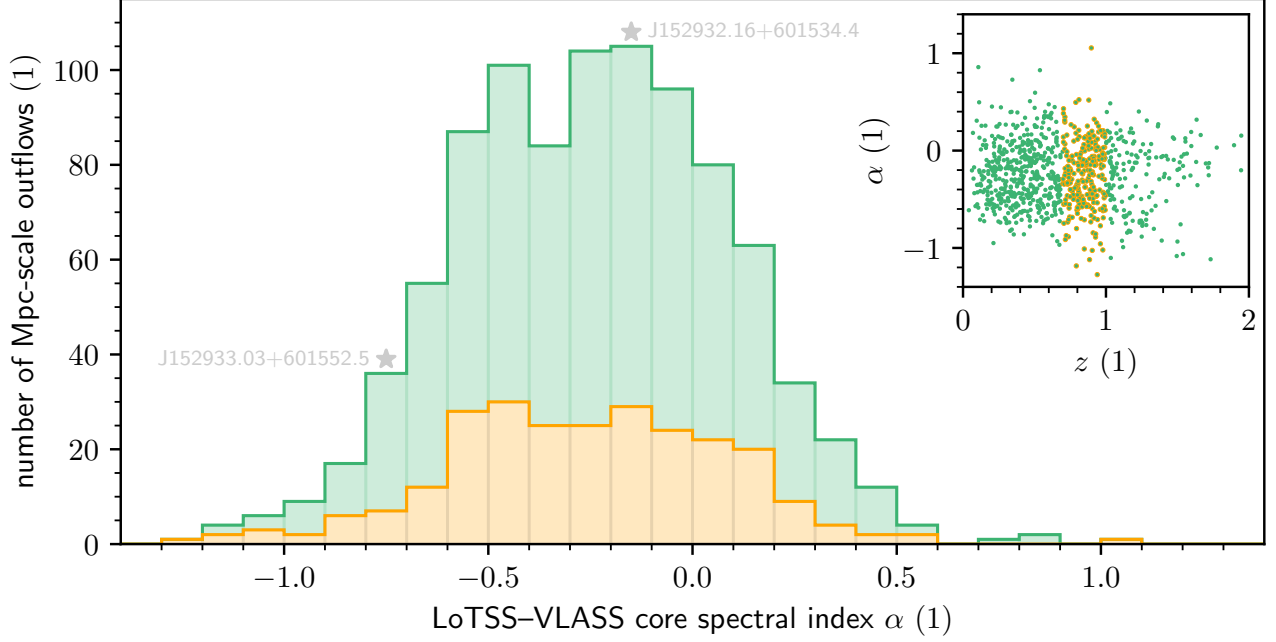
Extended Data Figure 3: **Rest-frame ultraviolet–optical spectroscopy of J152933.03+601552.5.** (This is the quasar-hosting galaxy 19'' north-northeast of Porphyrion’s host galaxy.) We identify redshifted hydrogen, carbon, oxygen, neon, and magnesium lines, jointly implying $z_s = 0.799 \pm 0.001$. Forbidden lines from the quasar’s narrow-line region are shown in red. The spectrum has been measured with the LRIS on the W. M. Keck Observatory’s Keck I Telescope.



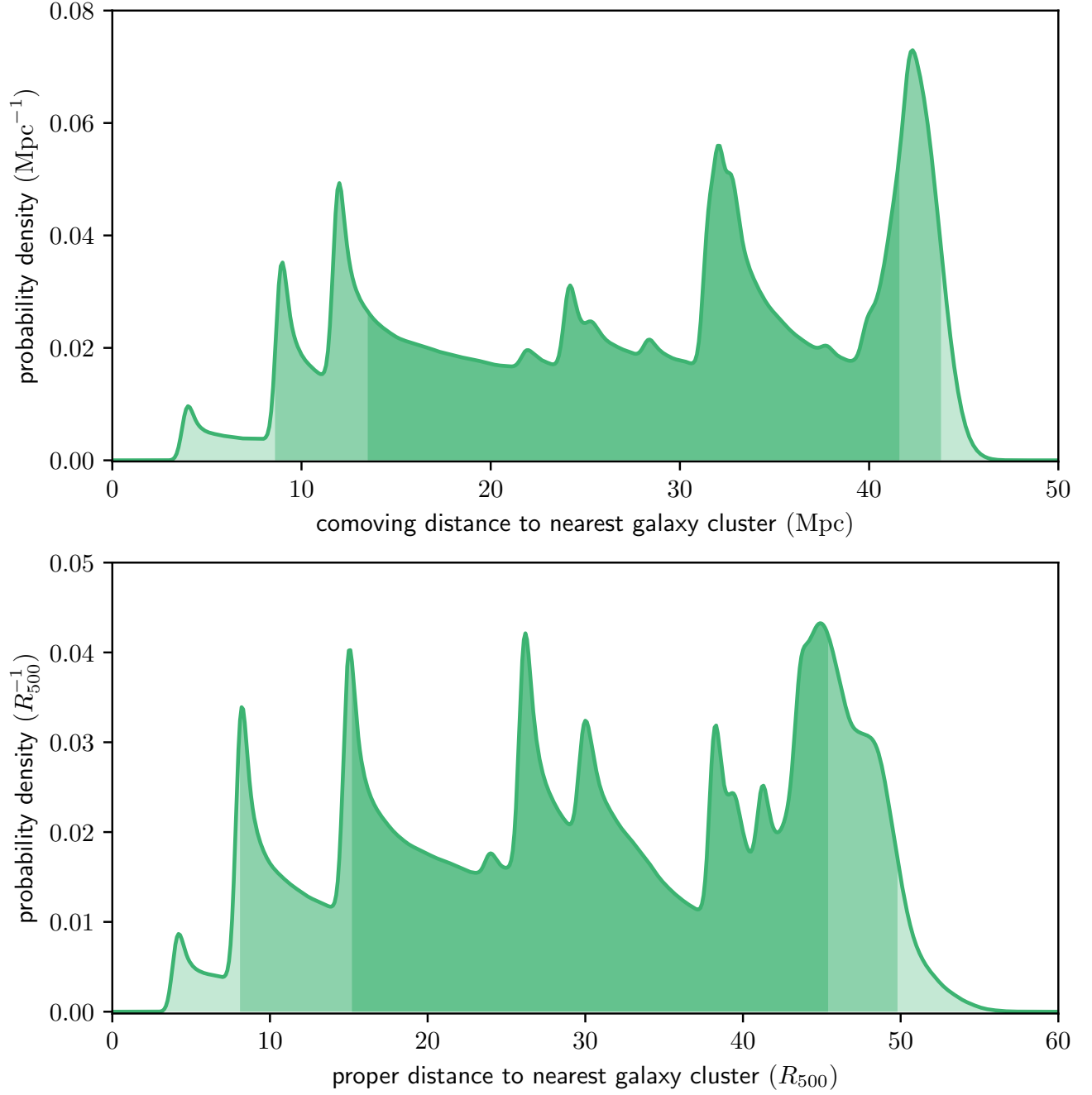
Extended Data Figure 4: **Astrometric offsets for Porphyrion's host galaxy.** All flux densities used in the inference of the host galaxy SED occur within an arcsecond of the Legacy DR10-identified host position. Coloured disks show 1σ (s.d.) astrometric uncertainties, while grey circles denote angular distances from the Legacy DR10-identified host position. The golden stars mark all other Legacy DR10-identified sources in the angular vicinity of Porphyrion's host.



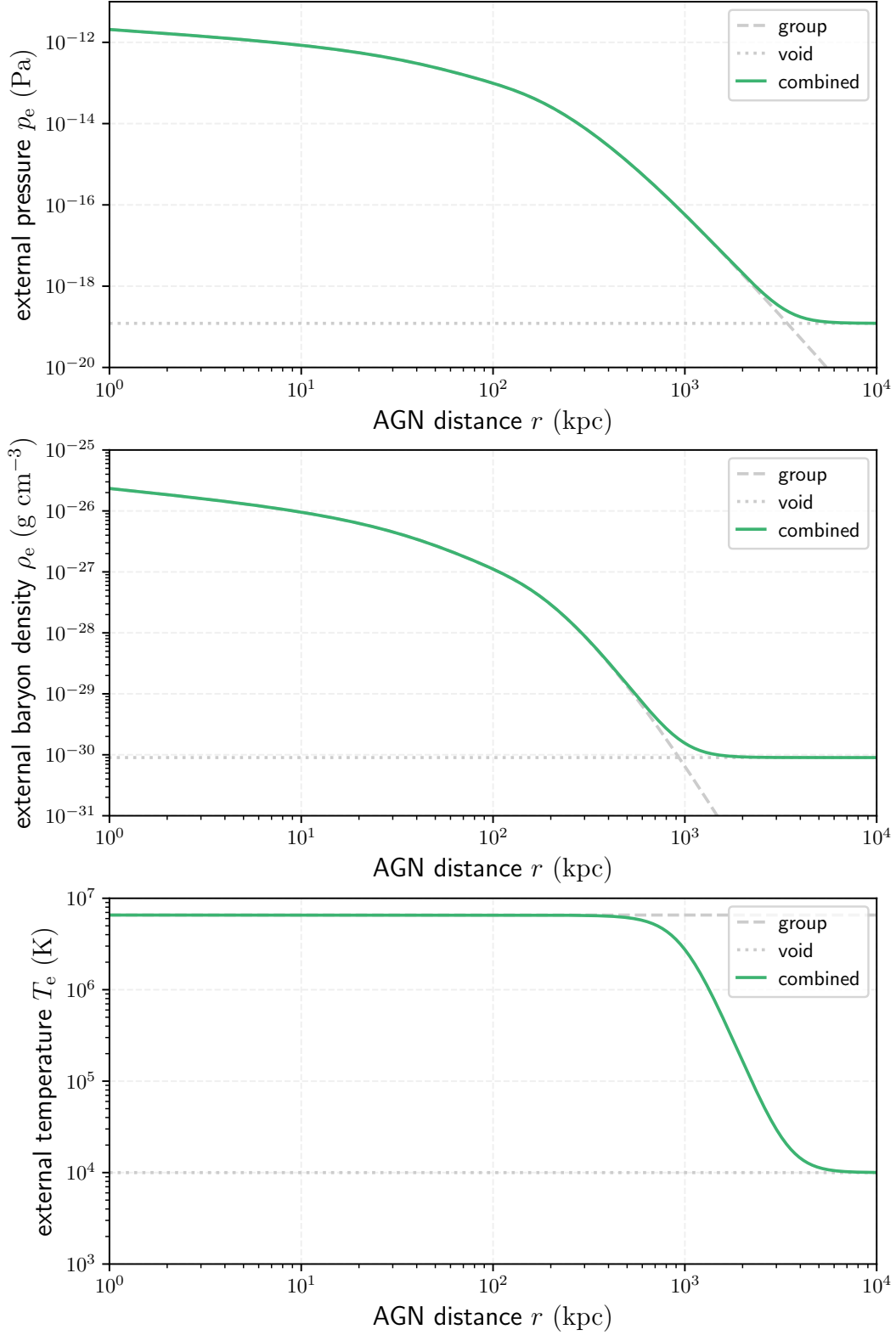
Extended Data Figure 5: **Radio spectral indices around Porphyrior's centre and southern tip.** The top panel, which covers $3' \times 3'$, reveals synchrotron self-absorption at metre wavelengths in the host galaxy, consistent with the fuelling of powerful jets. The bottom panel, which covers $2' \times 2'$, reveals a hotspot with backflow. We show effective spectral indices α between 0.46–2.08 m, at a resolution of $6.2''$. From light to dark, the contours denote thermal noise-induced spectral index uncertainties (s.d.) of 0.05, 0.1, 0.2, and 0.3.



Extended Data Figure 6: **Radio spectral index distributions of the cores of Mpc-scale outflows.** Using LoTSS and VLASS data, we determined 924 effective spectral indices α between 0.1–2.08 m. In grey, we indicate the bins in which the core spectral indices of J152932.16+601534.4, Porphyryon’s claimed host galaxy, and J152933.03+601552.5 fall. The distribution suggests that the spectral index of J152932.16+601534.4 ($\alpha = -0.18 \pm 0.06$) is more typical of Mpc-scale outflows than the spectral index of J152933.03+601552.5. (For J152933.03+601552.5, due to a VLASS non-detection, we show the LoTSS–uGMRT Band 4 spectral index.) The inset shows the same data as a function of redshift z . The golden subsample comprises Mpc-scale outflows whose redshifts differ at most $\Delta z = 0.1$ from those of either J152932.16+601534.4 or J152933.03+601552.5.



Extended Data Figure 7: **Probabilistic analysis of the distance to the nearest cluster.** DESI Legacy Imaging Surveys DR10 galaxy cluster redshift uncertainties induce multimodal, asymmetric probability distributions over measures of distance between Porphyrior's host galaxy and the nearest galaxy cluster. We mark median-centred intervals containing 68% and 95% of all probability. The data suggest that Porphyrior does not originate from a cluster.



Extended Data Figure 8: **Environmental profiles assumed in our dynamical modelling.** We show the pressure, baryon density, and temperature external to the outflow as a function of proper (rather than comoving) distance from Porphyryon's AGN. The profiles consist of contributions from the outflow's presumed galaxy group and the adjacent voids.

Extended Data Table 1: **Flux densities F_ν of Porphyryion’s host galaxy.** These are as measured, and thus have not been corrected for Galactic extinction. To allow the reader to do so, we provide estimated Galactic transmission fractions f_t . The uncertainties denote 1σ (s.d.). Entries are sorted by the central wavelengths λ of the observing bands, which cover the electromagnetic spectrum from the optical to the radio.¹

Band	λ (μm)	F_ν (Jy)	f_t (%)
Legacy g	$4.8 \cdot 10^{-1}$	$2.6 \pm 0.2 \cdot 10^{-6}$	96.3
Legacy r	$6.3 \cdot 10^{-1}$	$8.4 \pm 0.4 \cdot 10^{-6}$	97.5
Legacy z	$9.1 \cdot 10^{-1}$	$4.31 \pm 0.08 \cdot 10^{-5}$	98.6
Pan-STARRS i	$7.5 \cdot 10^{-1}$	$1.1 \pm 0.1 \cdot 10^{-5}$	98.0
Pan-STARRS y	$9.6 \cdot 10^{-1}$	$3.3 \pm 0.3 \cdot 10^{-5}$	98.7
WISE W ₁	$3.4 \cdot 10^0$	$2.41 \pm 0.02 \cdot 10^{-4}$	99.8
WISE W ₂	$4.6 \cdot 10^0$	$2.53 \pm 0.05 \cdot 10^{-4}$	99.9
WISE W ₃	$1.2 \cdot 10^1$	$8.1 \pm 0.5 \cdot 10^{-4}$	100
WISE W ₄	$2.2 \cdot 10^1$	$3.6 \pm 0.4 \cdot 10^{-3}$	100
VLASS	$1.0 \cdot 10^5$	$1.4 \pm 0.2 \cdot 10^{-3}$	100
FIRST	$2.1 \cdot 10^5$	$1.6 \pm 0.1 \cdot 10^{-3}$	100
uGMRT Band 4	$4.6 \cdot 10^5$	$2.1 \pm 0.1 \cdot 10^{-3}$	100
LoTSS	$2.1 \cdot 10^6$	$2.4 \pm 0.2 \cdot 10^{-3}$	100

When multiple flux densities or magnitudes from the same band were available in literature catalogues, we picked the highest signal-to-noise ratio measurement. Legacy data come from Dey *et al.* [18], Pan-STARRS data from Chambers *et al.* [26], WISE data from Lang *et al.* [52], VLASS data from Gordon *et al.* [53], FIRST data from Helfand *et al.* [54], uGMRT data from the present work, and LoTSS data from Shimwell *et al.* [4].